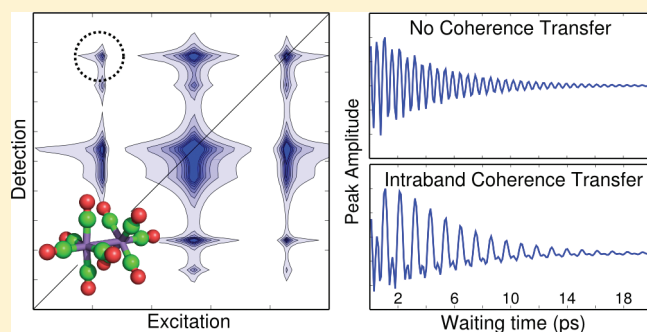


# Molecular Theory and Simulation of Coherence Transfer in Metal Carbonyls and Its Signature on Multidimensional Infrared Spectra

Carlos R. Baiz, Kevin J. Kubarych, and Eitan Geva\*

Department of Chemistry, University of Michigan, Ann Arbor, Michigan 48109, United States

**ABSTRACT:** We present a general and comprehensive theoretical and computational framework for modeling ultrafast multidimensional infrared spectra of a vibrational excitonic system in liquid solution. Within this framework, we describe the dynamics of the system in terms of a quantum master equation that can account for population relaxation, dephasing, coherence-to-coherence transfer, and coherence-to-population transfer. A unique feature of our approach is that, in principle, it does not rely on any adjustable fitting parameters. More specifically, the anharmonic vibrational Hamiltonian is derived from ab initio electronic structure theory, and the system–bath coupling is expressed explicitly in terms of liquid degrees of freedom whose dynamics can be obtained via molecular dynamics simulations. The applicability of the new approach is demonstrated by employing it to model the recently observed signatures of coherence transfer in the two-dimensional spectra of dimanganese decacarbonyl in liquid cyclohexane. The results agree well with experiment and shed new light on the nature of the molecular interactions and dynamics underlying the spectra and the interplay between dark and bright states, their level of degeneracy, and the nature of their interactions with the solvent.



## I. INTRODUCTION

Coherent multidimensional infrared spectroscopy has recently become a powerful technique for unraveling structure–dynamics relationships in many complex systems with femtosecond time resolution.<sup>1–10</sup> Similar to multidimensional NMR spectroscopy,<sup>11</sup> detailed molecular information is most often derived from models that map structures to frequencies, and the quality of the specific model largely determines the amount of molecular information that can be extracted from the experiment.<sup>12–16</sup> The ability of multidimensional NMR to provide atomistically detailed structural information in large biomolecules emerges from the fact that nuclear spin resonances and spin–spin couplings can be predicted quantitatively from standard models, providing the structure–frequency map needed to translate the experimental data into chemical structures.<sup>17</sup> Similarly, the most insightful two-dimensional infrared (2DIR) experiments to date use complex models in order to obtain information on the molecular structure and dynamics underlying the spectra. For example, 2DIR studies of peptides in the amide-I region rely on a combination of molecular dynamics simulations, high-quality ab initio frequency maps, and vibrational coupling schemes to extract protein structures from the measured spectra.<sup>18–24</sup>

Although frequency maps have proven successful in reproducing the experimental lineshapes, two-dimensional spectra also contain information on such processes as coherence-to-coherence transfer<sup>25,26</sup> or relaxation to dark states, for which

reliable microscopic models remain underdeveloped. As a result, the analysis of these processes is often based on phenomenological and somewhat oversimplified models that contain a limited amount of information on the underlying molecular picture. It is therefore important to construct a theoretical framework to account for the aforementioned processes based on an explicit description of molecular structure and dynamics.

Over the last ten years, metal carbonyls have been established as useful benchmark systems for 2DIR spectroscopy.<sup>27–38</sup> Their rich vibrational structure, narrow lineshapes, and large oscillator strengths make metal carbonyls ideal molecules for testing different aspects of 2DIR spectroscopy, such as intramolecular vibrational redistribution (IVR), where populations are transferred among high-frequency vibrational states within the molecule, or vibrational energy relaxation (VER), where the energy is lost to the bath or low frequency modes of the molecule. In addition, newer experiments have been able to directly test coherence–coherence coupling (coherence transfer), where a coherence created between two eigenstates by a laser pulse is spontaneously transferred to a different coherence of similar frequency but involving a new eigenstate or pair of eigenstates.

**Special Issue:** Shaul Mukamel Festschrift

**Received:** September 29, 2010

**Revised:** January 20, 2011

One system in particular  $\text{Rh}(\text{CO})_2\text{C}_5\text{H}_7\text{O}_2$  (RDC) has provided important insights on the effect of anharmonic coupling coefficients<sup>28,39</sup> and coherence transfer<sup>25,39–41</sup> on multidimensional spectra. The interpretation of the results, however, relied on fitting the data to phenomenological models which lacked molecular detail. Furthermore, as the number of fitting parameters grows rapidly with the number of modes, phenomenological models become impractical for most systems, which unlike RDC would typically have more than two modes.

Within this context, recent effort has been directed toward developing a general electronic-structure-based framework for calculating anharmonic frequencies and oscillator strengths, which can be compared directly to experiment.<sup>35,36,42</sup> It is important to note that although the 2DIR experiment only probes the bright (i.e., IR active) modes directly, it was found necessary to include the dark (i.e., IR inactive) modes which remain strongly coupled and turn out to have a significant effect on the transition frequencies and dipole moments. In the present paper we attempt to develop a new and complementary general framework aimed at providing a molecularly detailed description of solvent-induced dynamical effects such as dephasing, population relaxation, coherence-to-coherence transfer and population-to-coherence transfer. The development of such a framework is motivated in part by recent 2DIR measurements of the carbonyl stretching modes of dimanganese decacarbonyl, ( $\text{Mn}_2(\text{CO})_{10}$ ; DMDC) where direct signatures of coherence transfer were observed in the spectra.<sup>26</sup> The strong infrared transitions and weakly interacting cyclohexane solvent allowed for the observation of long-lived coherences between singly excited states as well as dual-frequency oscillations of certain 2D cross peaks during the waiting time. The latter observation was, to the best of our knowledge, the first unambiguous evidence for low-frequency coherence transfer in vibrational systems. It is worth pointing out that RDC only has two carbonyl stretching modes and two states in the singly excited band and, thus, only one low-frequency coherence. The observation of coupling between coherences within the singly excited band requires a system consisting of at least three distinct energy levels, which is the case for DMDC. In this paper we present a theoretical and computational modeling approach based on a Markovian quantum master equation, which, in addition to the coherence and population relaxation terms, also accounts for coherence-to-coherence transfer as well as coherence-to-population and population-to-coherence transfer.

Importantly, our approach does not rely on empirical adjustable parameters: we obtain the transition frequencies and dipole moments from electronic-structure calculations and employ explicit expressions for the relaxation matrix elements in terms of solvent force correlation functions, which are in turn obtained from molecular dynamics simulations. We subsequently use the model to explore the vibrational spectroscopy of  $\text{Mn}_2(\text{CO})_{10}$  with particular attention to the effects of coherence transfer and coherence-population coupling on the spectra as well as investigate the effect of strongly coupled dark modes on the lineshapes and waiting-time dependence of the 2D peaks.

The paper is organized as follows. In section II, we describe the molecular Hamiltonian and derive the quantum master equation. In section III we derive explicit expressions for the system–bath coupling. In sections IV and V, we provide a treatment of the field-matter coupling and outline the procedure for computing multidimensional spectra. In section VI, we provide the specific

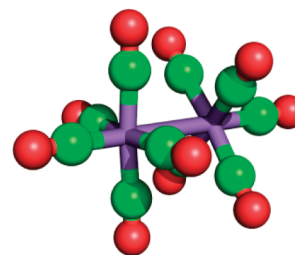


**Figure 1.** Equilibrium structure of dimanganese decacarbonyl ( $\text{Mn}_2(\text{CO})_{10}$ , DMDC), where the green and red atoms represent carbon and oxygen, respectively.

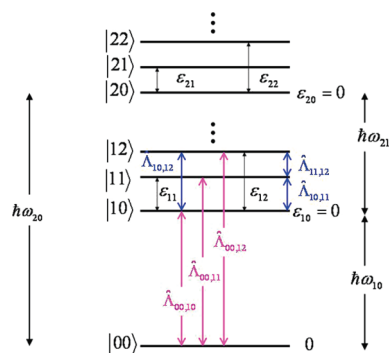


**Figure 2.** Schematic view of the system energy level diagram and some of the bath operators associated with various transitions. The interband and intraband transitions are marked in blue and pink, respectively. The bath-operators associated with the interband transitions (pink) are neglected in this paper. See Figure 3 for a schematic view of the density matrix.

simulation parameters, and in sections VII and VIII, we discuss the simulation results for  $\text{Mn}_2(\text{CO})_{10}$  in comparison to experiment. Finally, in section IX, we summarize the results and provide an outlook toward future uses of the model.

## II. EXCITONIC VIBRATIONAL HAMILTONIAN AND QUANTUM MASTER EQUATION

In this section we develop the theoretical framework for modeling coherence transfer in an excitonic system. For the sake of concreteness, the theory is developed in the context of the 2DIR spectroscopy of the 10-carbonyl system  $\text{Mn}_2(\text{CO})_{10}$  (Figure 1) in the terminal  $\text{C}\equiv\text{O}$  stretching region. However, it should be noted that the methodologies described herein can be straightforwardly extended to other molecular systems.

We start by writing the overall system Hamiltonian in a system–bath form

$$\hat{H} = \hat{H}_S + \hat{H}_B + \hat{H}_{BS} \quad (1)$$

The system Hamiltonian,  $\hat{H}_S$ , corresponds to the *anharmonic* vibrational Hamiltonian of the  $\text{C}\equiv\text{O}$  stretches in DMDC

$$\hat{H}_S = \sum_{j=0}^{n_1-1} (\hbar\omega_{10} + \varepsilon_{1j}) |1j\rangle\langle 1j| + \sum_{j=0}^{n_2-1} (\hbar\omega_{20} + \varepsilon_{2j}) |2j\rangle\langle 2j| \quad (2)$$

Here,  $|\alpha j\rangle$  represents the  $j$ th state ( $j = 0, 1, 2, \dots$ ) in the  $\alpha$ th band, and  $\alpha = 0, 1, 2$  represents the ground, singly excited, and doubly excited states, respectively (Figure 2). Since the model is developed within the context of two-dimensional spectroscopy, only

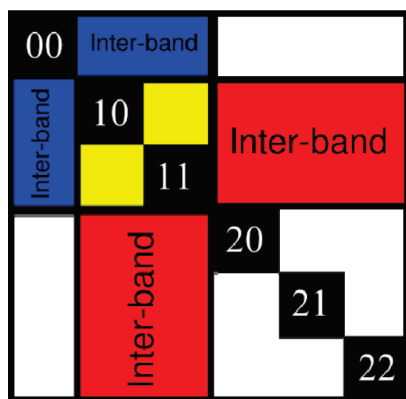


**Figure 3.** Schematic view of populations, interband (blue and red) and intraband coherence (yellow) blocks in the density matrix. The intraband coherences within the second manifold levels are inaccessible in 2DIR experiments, and thus are not shown.

the singly- and doubly excited states are considered as these are the only states that are accessed experimentally. The ground state is denoted by  $|00\rangle$  and its energy is assumed to coincide with the energy origin.  $n_1$  is the number of C≡O stretch modes, where it should be understood that all C≡O stretches need to be included, whether photoactive or not ( $n_1 = 10$  in the case of DMDC).  $n_1$  is also the number of states in the “singly-excited” band. The overall number of “doubly-excited” states is  $n_2 = n_1(n_1 + 1)/2$  (55 in the case of DMDC). Importantly, the “singly-excited” and “doubly-excited” states correspond to eigenfunctions of the anharmonic vibrational Hamiltonian, and as such include contributions from harmonic states with higher occupancy. We also assume that the energy levels within the  $\alpha$ -th band are ordered in the following manner:  $\varepsilon_{\alpha 0} \leq \varepsilon_{\alpha 1} \leq \varepsilon_{\alpha 2} \leq \dots$  (see Figure 2). The transition frequencies and dipole moments are calculated from electronic structure methods. Indeed, we have recently shown that these can be obtained in the case of DMDC by combining density functional theory with vibrational perturbation theory.<sup>35,36</sup> Alternatively, if known, the experimental frequencies and anharmonicities may be used. It should be noted that, in a system like DMDC, the intraband transitions range from 0 to 135  $\text{cm}^{-1}$ , whereas the interband transition frequency is  $\sim 2000 \text{ cm}^{-1}$ . Thus, at room temperature, one can assume that

$$\varepsilon_{\alpha j} \leq k_B T \ll \hbar \omega_{\alpha \beta} \quad (3)$$

The bath Hamiltonian,  $\hat{H}_B$ , corresponds to the solvent degrees of freedom, and will remain undetermined for the time being. Finally, the system–bath coupling,  $\hat{H}_{BS}$ , in its most general form, is given by

$$\begin{aligned} \hat{H}_{BS} = & |00\rangle \hat{\Lambda}_{00,00} \langle 00| + \sum_{j=1}^{n_1-1} \sum_{k=1}^{n_1-1} |1j\rangle \hat{\Lambda}_{1j,1k} \langle 1k| \\ & + \sum_{j=1}^{n_2-1} \sum_{k=1}^{n_2-1} |2j\rangle \hat{\Lambda}_{2j,2k} \langle 2k| + \sum_{j=1}^{n_1-1} [|00\rangle \hat{\Lambda}_{00,1j} \langle 1j| \\ & + |1j\rangle \hat{\Lambda}_{1j,00} \langle 00|] + \sum_{k=1}^{n_2-1} [|00\rangle \hat{\Lambda}_{00,2k} \langle 2k| \\ & + |2k\rangle \hat{\Lambda}_{2k,00} \langle 00|] + \sum_{j=1}^{n_1-1} \sum_{k=1}^{n_2-1} [|1j\rangle \hat{\Lambda}_{1j,2k} \langle 2k| \\ & + |2k\rangle \hat{\Lambda}_{2k,1j} \langle 1j|] \end{aligned} \quad (4)$$

Here,  $\{\hat{\Lambda}_{\alpha j \beta k}\}$  are the, yet to be explicitly specified, bath operators. Now, consider the free bath equilibrium density operator,  $\hat{\rho}_B^{\text{eq}} = \exp(-\beta \hat{H}_B) / \text{Tr}_B[\exp(-\beta \hat{H}_B)]$  where  $\beta = 1/k_B T$ . Since  $\text{Tr}_B[\hat{H}_{BS} \hat{\rho}_B^{\text{eq}}]$ , is a system operator, it can be added to the system Hamiltonian, so that  $\hat{H}_S \rightarrow \hat{H}_S + \text{Tr}_B[\hat{H}_{BS} \hat{\rho}_B^{\text{eq}}]$ . As a result, the system–bath coupling is also need to be renormalized so that  $\hat{H}_{BS} \rightarrow \hat{H}_{BS} - \text{Tr}_B[\hat{H}_{BS} \hat{\rho}_B^{\text{eq}}]$ . Thus, we can assume, without loss of generality, that  $\text{Tr}_B[\hat{H}_{BS} \hat{\rho}_B^{\text{eq}}] \equiv \langle \hat{H}_{BS} \rangle_B = 0$ , which implies that

$$\text{Tr}_B[\hat{\Lambda}_{\alpha j, \beta k} \hat{\rho}_B^{\text{eq}}] \equiv \langle \hat{\Lambda}_{\alpha j, \beta k} \rangle_B = 0 \quad \text{for all } \alpha j, \beta k \quad (5)$$

Noting that  $\hat{\Lambda}_{\alpha j \beta k}$  is the bath operator that couples to the system operator  $|\alpha j\rangle \langle \beta k|$  and assuming that the bath is weakly coupled to the system, energy conservation dictates that  $\hat{\Lambda}_{\alpha j \beta k}$  induces an energy change in the bath which is comparable to  $|E_{\alpha j} - E_{\beta k}|$ . The fact that all modes that are close to resonance with the photoactive transitions are included in the system Hamiltonian then implies that the system–bath interactions are of the nonresonant type. Thus, the bath can exchange no more than  $\sim k_B T$  with the system. Since interband energy gaps are much larger than  $k_B T$ , one can neglect the interband system–bath coupling terms in eq 4, thereby considerably simplifying the system–bath coupling equation

$$\begin{aligned} \hat{H}_{BS} = & |00\rangle \hat{\Lambda}_{00,00} \langle 00| + \sum_{j=1}^{n_1-1} \sum_{k=1}^{n_1-1} |1j\rangle \hat{\Lambda}_{1j,1k} \langle 1k| \\ & + \sum_{j=1}^{n_2-1} \sum_{k=1}^{n_2-1} |2j\rangle \hat{\Lambda}_{2j,2k} \langle 2k| \end{aligned} \quad (6)$$

In what follows, we will refer to this approximation as the *intraband coupling approximation* (IntraCA).

Next, assuming that the system starts out at thermal equilibrium,  $\hbar \omega_{10} \gg k_B T$  implies that the initial state of the overall system is given by the following density operator:

$$\hat{\rho}(0) = \hat{\rho}_B^{\text{eq}} \otimes |00\rangle \langle 00| \equiv \hat{\rho}_B^{\text{eq}} \otimes \hat{\sigma}(0) \quad (7)$$

Here,  $\hat{\sigma}(t) = \text{Tr}_B[\hat{\rho}(t)]$  is the reduced density operator of the system. In practice it is convenient to represent  $\hat{\sigma}(t)$  as a matrix in the basis of the system eigenfunctions,  $\{|\alpha j\rangle\}$ . In what follows we will refer to the diagonal elements,  $\{\sigma_{\alpha j \alpha j}(t)\}$ , and off-diagonal elements  $\{\sigma_{\alpha j \beta k}(t)\}$ , as *populations* and *coherences*, respectively. We will also distinguish between *intraband coherences*,  $\{\sigma_{\alpha j, \alpha k}(t)\}$ , and *interband coherences*,  $\{\sigma_{\alpha j, \beta k}(t)\}$  (where  $\alpha \neq \beta$ ).

The reduced dynamics of the system  $\hat{\sigma}(t)$  are described by a quantum master equation (QME) which can be derived in the limit of weak system–bath coupling by assuming Markovity (i.e., that the time scale for system relaxation is slower than the relevant bath correlation times).<sup>43–67</sup> The resulting QMEs for the populations, intraband and interband coherences are given below

$$\begin{aligned} \frac{d}{dt} \sigma_{\alpha j, \alpha j}(t) = & - \sum_{m \neq j} k_{\alpha m} - \alpha_j \sigma_{\alpha j, \alpha j}(t) \\ & + \sum_{m \neq j} k_{\alpha j} - \alpha_m \sigma_{\alpha m, \alpha m}(t) \\ & - \sum_{m \neq j, n} \Gamma_{\alpha j, \alpha n; \alpha n, \alpha m}(\omega_{\alpha m, \alpha n}) \sigma_{\alpha m, \alpha j}(t) \\ & - \sum_{m \neq j, n} \Gamma_{\alpha j, \alpha n; \alpha n, \alpha m}^*(\omega_{\alpha m, \alpha n}) \sigma_{\alpha j, \alpha m}(t) \\ & + \sum_{m \neq n} \Gamma_{\alpha n, \alpha j; \alpha j, \alpha m}(\omega_{\alpha m, \alpha j}) \sigma_{\alpha m, \alpha n}(t) \\ & + \sum_{m \neq n} \Gamma_{\alpha n, \alpha j; \alpha j, \alpha m}^*(\omega_{\alpha m, \alpha j}) \sigma_{\alpha n, \alpha m}(t) \end{aligned} \quad (8)$$

$$\begin{aligned}
\frac{d}{dt} \sigma_{\alpha_j, \alpha_k}(t) = & - \left\{ i\omega_{\alpha_j, \alpha_k} \sigma_{\alpha_j, \alpha_k}(t) + \sum_{n \neq j} \Gamma_{\alpha_j, \alpha_n; \alpha_n, \alpha_j}(\omega_{\alpha_j, \alpha_n}) \right. \\
& + \sum_{m \neq k} \Gamma_{\alpha_k, \alpha_m; \alpha_m, \alpha_k}(\omega_{\alpha_k, \alpha_m}) + \Gamma_{\alpha_j, \alpha_j; \alpha_j, \alpha_j}(0) \\
& + \Gamma_{\alpha_k, \alpha_k; \alpha_k, \alpha_k}(0) - \Gamma_{\alpha_k, \alpha_k; \alpha_j, \alpha_j}(0) \\
& \left. - \Gamma_{\alpha_j, \alpha_j; \alpha_k, \alpha_k}(0) \right\} \sigma_{\alpha_j, \alpha_k}(t) \\
& - \sum_{m \neq (j, k)} \left[ \sum_n \Gamma_{\alpha_j, \alpha_n; \alpha_n, \alpha_m}(\omega_{\alpha_m, \alpha_n}) \right] \sigma_{\alpha_m, \alpha_k}(t) \\
& - \sum_{m \neq (j, k)} \left[ \sum_n \Gamma_{\alpha_k, \alpha_n; \alpha_n, \alpha_m}(\omega_{\alpha_m, \alpha_n}) \right] \sigma_{\alpha_j, \alpha_m}(t) \\
& + \sum_{m \neq n, m \neq j, n \neq k} \Gamma_{\alpha_n, \alpha_k; \alpha_j, \alpha_m}(\omega_{\alpha_m, \alpha_j}) \sigma_{\alpha_m, \alpha_n}(t) \\
& + \sum_{m \neq n, m \neq j, n \neq k} \Gamma_{\alpha_m, \alpha_j; \alpha_k, \alpha_n}(\omega_{\alpha_n, \alpha_k}) \sigma_{\alpha_m, \alpha_n}(t) \\
& - \left[ \sum_n \Gamma_{\alpha_j, \alpha_n; \alpha_n, \alpha_k}(\omega_{\alpha_k, \alpha_n}) \right] \sigma_{\alpha_k, \alpha_k}(t) \\
& - \left[ \sum_m \Gamma_{\alpha_k, \alpha_m; \alpha_m, \alpha_j}(\omega_{\alpha_j, \alpha_m}) \right] \sigma_{\alpha_j, \alpha_j}(t) \\
& + \sum_{m \neq (j, k)} \Gamma_{\alpha_m, \alpha_k; \alpha_j, \alpha_m}(\omega_{\alpha_m, \alpha_j}) \sigma_{\alpha_m, \alpha_m}(t) \\
& + \sum_{m \neq (j, k)} \Gamma_{\alpha_m, \alpha_j; \alpha_k, \alpha_m}(\omega_{\alpha_m, \alpha_k}) \sigma_{\alpha_m, \alpha_m}(t) \quad (9)
\end{aligned}$$

$$\begin{aligned}
\frac{d}{dt} \sigma_{\alpha_j, \beta_k}(t) = & - \left\{ i\omega_{\alpha_j, \beta_k} + \sum_{n \neq j} \Gamma_{\alpha_j, \alpha_n; \alpha_n, \alpha_j}(\omega_{\alpha_j, \alpha_n}) \right. \\
& + \sum_{n \neq k} \Gamma_{\beta_k, \beta_n; \beta_n, \beta_k}(\omega_{\beta_k, \beta_n}) + \Gamma_{\alpha_j, \alpha_j; \alpha_j, \alpha_j}(0) \\
& + \Gamma_{\beta_k, \beta_k; \beta_k, \beta_k}(0) - \Gamma_{\beta_k, \beta_k; \alpha_j, \alpha_j}(0) \\
& \left. - \Gamma_{\alpha_j, \alpha_j; \beta_k, \beta_k}(0) \right\} \sigma_{\alpha_j, \beta_k}(t) \\
& - \sum_{m \neq j} \left[ \sum_n \Gamma_{\alpha_j, \alpha_n; \alpha_n, \alpha_m}(\omega_{\alpha_m, \alpha_n}) \right] \sigma_{\alpha_m, \beta_k}(t) \\
& - \sum_{m \neq k} \left[ \sum_n \Gamma_{\beta_k, \beta_n; \beta_n, \beta_m}(\omega_{\beta_m, \beta_n}) \right] \sigma_{\alpha_j, \beta_m}(t) \\
& + \sum_{m \neq j, n \neq k} \Gamma_{\beta_n, \beta_k; \alpha_j, \alpha_m}(\omega_{\alpha_m, \alpha_j}) \sigma_{\alpha_m, \beta_n}(t) \\
& + \sum_{m \neq j, n \neq k} \Gamma_{\alpha_m, \alpha_j; \beta_k, \beta_n}(\omega_{\beta_n, \beta_k}) \sigma_{\alpha_m, \beta_n}(t) \quad (10)
\end{aligned}$$

Here,

$$\Gamma_{\alpha_j, \alpha_k; \beta_m, \beta_n}(\omega) = \frac{1}{\hbar^2} \int_0^\infty d\tau e^{i\omega\tau} C_{\alpha_j, \alpha_k; \beta_m, \beta_n}(\tau) \quad (11)$$

where  $\{C_{\alpha_j, \alpha_k; \beta_m, \beta_n}(\tau)\}$  are free-bath quantum-mechanical correlation functions

$$\begin{aligned}
C_{\alpha_j, \alpha_k; \beta_m, \beta_n}(\tau) &= \text{Tr}_B[\hat{\rho}_B^{\text{eq}} e^{iH_B\tau/\hbar} \hat{\Lambda}_{\alpha_j, \alpha_k} e^{-iH_B\tau/\hbar} \hat{\Lambda}_{\beta_m, \beta_n}] \\
&\equiv \langle \hat{\Lambda}_{\alpha_j, \alpha_k}(\tau) \hat{\Lambda}_{\beta_m, \beta_n} \rangle_B \quad (12)
\end{aligned}$$

and

$$k_{\alpha_m \leftarrow \alpha_j} = 2\text{Re}[\Gamma_{\alpha_j, \alpha_m; \alpha_m, \alpha_j}(\omega_{\alpha_j, \alpha_m})] \quad (13)$$

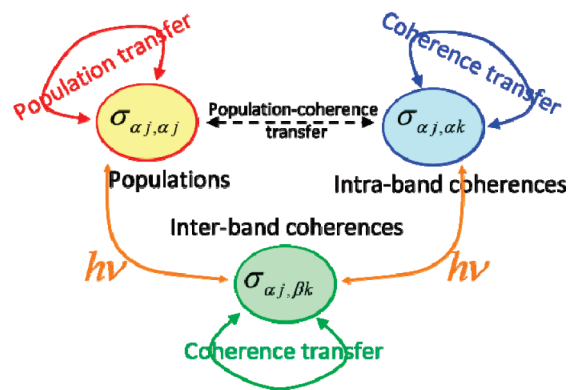


**Figure 4.** Schematic representation of the vibrational dynamics captured by the model. Interband coherences are decoupled from intraband coherences and populations. Intraband coherences are coupled to populations. The light–matter interactions couple populations and intraband coherences to interband coherences.

are intraband population relaxation rate constants. It should be noted that within our model, interband population relaxation is assumed infinitely slow, due to the IntraCA. However, it is also important to note that population transfer between bright and dark modes is accounted for and is expected to be the dominant mechanism for population relaxation.

Importantly, the QMEs (eqs 8–10) were derived without neglecting terms that couple between coherences and populations as well as terms that couple between different coherences. The latter terms, in turn, lead to *coherence transfer*. Note that these couplings are both induced. Within the IntraCA, populations are only coupled to intraband coherences and intraband coherences are not coupled to interband coherences. Thus, the coherence transfer terms can be further classified as *intraband* or *interband coherence transfer*, depending on the type of coherences that are coupled (see Figure 4).

### III. SYSTEM–BATH COUPLING

In practice, one needs to know the bath operators that couple to the system in order to describe its dynamics in terms of the QMEs in eqs 8–10. To this end, we note that the Hamiltonian of the overall system is generally given by

$$H(\mathbf{q}, \mathbf{p}, \mathbf{Q}, \mathbf{P}) = H_S^0(\mathbf{q}, \mathbf{p}) + T(\mathbf{P}) + V_0(\mathbf{Q}) + V_1(\mathbf{q}, \mathbf{Q}) \quad (14)$$

Here,  $\mathbf{Q} = (Q_1, \dots, Q_N)$  are the bath coordinates and  $\mathbf{q} = (q_1, \dots, q_{n_1})$  are the normal mode coordinates,  $\mathbf{P} = (P_1, \dots, P_N)$  and  $\mathbf{p} = (p_1, \dots, p_{n_1})$  are the corresponding conjugate momenta,  $H_S^0(\mathbf{q}, \mathbf{p})$  is the gas phase vibrational Hamiltonian,  $T(\mathbf{P})$  is the bath kinetic energy,  $V_0(\mathbf{Q})$  is the free bath potential energy (i.e., solvent–solvent interactions), and  $V_1(\mathbf{q}, \mathbf{Q})$  represent the interactions between the bath and the system (i.e., solvent–solute interactions). It should be noted that the explicit functional form of  $V_0(\mathbf{Q})$  and  $V_1(\mathbf{q}, \mathbf{Q})$  depends on the force fields governing solvent–solvent and solvent–solute interactions which are system specific.

Since the displacement along the normal mode coordinates is expected to be relatively small in a molecule like DMDC, one can approximate  $V_1(\mathbf{q}, \mathbf{Q})$  by its expansion to first order in the normal

mode coordinates

$$\begin{aligned} V_1(\mathbf{q}, \mathbf{Q}) &= V_1(\mathbf{Q}, 0) + \sum_{l=1}^{n_1} \left[ \frac{\partial V_1}{\partial q_l} \right]_{\mathbf{q}=0} q_l + \dots \\ &\equiv V_1(\mathbf{Q}, 0) - \sum_{l=1}^{n_1} F_l(\mathbf{Q}) q_l + \dots \end{aligned} \quad (15)$$

Here,  $F_l(\mathbf{Q})$  is the force exerted by the bath on the  $l$ th normal mode.

Since  $V_1(\mathbf{Q}, 0)$  is a bath operator, it can be included in the potential energy part of the bath Hamiltonian, so that

$$H_B(\mathbf{Q}, \mathbf{P}) = T(\mathbf{P}) + V_0(\mathbf{Q}) + V_1(0, \mathbf{Q}) \quad (16)$$

It is also convenient to define the free bath thermal average of the force  $F_l(\mathbf{Q})$

$$\langle F_l(\mathbf{Q}) \rangle_B = \frac{\text{Tr}[F_l(\hat{\mathbf{Q}}) \exp(-\beta \hat{H}_B)]}{\text{Tr}[\exp(-\beta \hat{H}_B)]} \quad (17)$$

so that the system Hamiltonian and the system–bath coupling can be defined as follows:

$$H_S(\mathbf{q}, \mathbf{p}) = H_S^0(\mathbf{q}, \mathbf{p}) - \sum_{l=1}^{n_1} \langle F_l(\mathbf{Q}) \rangle_B q_l \quad (18)$$

$$\begin{aligned} H_{BS} &= - \sum_{l=1}^{n_1} (F_l(\mathbf{Q}) - \langle F_l(\mathbf{Q}) \rangle_B) q_l \\ &\equiv - \sum_{l=1}^{n_1} \delta F_l(\mathbf{Q}) q_l \end{aligned} \quad (19)$$

Writing  $H_{BS}$  in terms of the eigenfunctions of  $\hat{H}_S$  and only accounting for intraband coupling we obtain (see eq 6)

$$\begin{aligned} \hat{H}_{BS} &= |00\rangle \left[ \sum_{l=1}^{n_1} q_{l:00,00} \delta F_l(\mathbf{Q}) \right] \langle 00| \\ &+ \sum_{j=0}^{n_1-1} |1j\rangle \left[ \sum_{l=1}^{n_1} q_{l:1j,1j} \delta F_l(\mathbf{Q}) \right] \langle 1j| \\ &+ \sum_{j=1}^{n_2-1} |2j\rangle \left[ \sum_{l=1}^{n_1} q_{l:2j,2j} \delta F_l(\mathbf{Q}) \right] \langle 2j| \\ &+ \sum_{j \neq k}^{n_1-1} |1j\rangle \left[ \sum_{l=1}^{n_1} q_{l:1j,1k} \delta F_l(\mathbf{Q}) \right] \langle 1k| \\ &+ \sum_{j \neq k}^{n_2-1} |2j\rangle \left[ \sum_{l=1}^{n_1} q_{l:2j,2k} \delta F_l(\mathbf{Q}) \right] \langle 2k| \end{aligned} \quad (20)$$

where

$$q_{l:\alpha j, \alpha k} = \langle \alpha j | q_l | \alpha k \rangle \quad (21)$$

It should be noted that  $q_{l:\alpha j, \alpha k} = 0$  if the vibrational Hamiltonian is assumed harmonic, i.e. within the normal mode approximation. Thus, within the treatment of the system–bath coupling as linear in the normal mode coordinates, one needs to use the anharmonic vibrational Hamiltonian in order to account for relaxation.

According to eq 20 one can identify the bath operators that couple to the system as so

$$\begin{aligned} \Lambda_{00,00} &= \sum_{l=1}^{n_1} q_{l:00,00} \delta F_l(\mathbf{Q}); & \Lambda_{1j,1j} &= \sum_{l=1}^{n_1} q_{l:1j,1j} \delta F_l(\mathbf{Q}); \\ \Lambda_{2j,2j} &= \sum_{l=1}^{n_1} q_{l:2j,2j} \delta F_l(\mathbf{Q}); & \Lambda_{1j,1k} &= \sum_{l=1}^{n_1} q_{l:1j,1k} \delta F_l(\mathbf{Q}); \\ \Lambda_{2j,2k} &= \sum_{l=1}^{n_1} q_{l:2j,2k} \delta F_l(\mathbf{Q}) \end{aligned} \quad (22)$$

The corresponding bath correlation functions then assume the following form:

$$\langle \Lambda_{\alpha j, \alpha k}(t) \Lambda_{\beta m, \beta n} \rangle = \sum_{l, l'=1}^{n_1} q_{l:\alpha j, \alpha k} q_{l':\beta m, \beta n} \langle \delta F_l(t) \delta F_{l'} \rangle \quad (23)$$

In principle, if the force fields for the solvent–solute interactions are known, and then the forces  $\{F_l\}$  can be obtained explicitly. Furthermore, due to the IntraCA,  $\{\Gamma_{\alpha j, \alpha k; \beta m, \beta n}(\omega)\}$  only need to be calculated at frequencies which are comparable to or smaller than  $k_B T / \hbar$  (see eq 11). Thus, the corresponding correlation functions,  $\{C_{\alpha j, \alpha k; \beta m, \beta n}(\tau)\}$ , can be obtained from classical MD simulations where the solute and solvent are treated as rigid molecules. It should be noted that the assumption that the solvent dynamics are independent of the solute vibrational state is implicit in the derivation of the QME and requires that the system–bath coupling is sufficiently weak.

One can further simplify the model by making the following plausible assumption:

$$\langle \delta F_l(t) \delta F_{l'} \rangle \approx \delta(l, l') C_{FF}(t) \quad (24)$$

Equation 24 relies on the assumption that the forces on different normal modes are uncorrelated but have the same autocorrelation function (which can be justified in a molecule like DMDC where the CO stretch normal modes are highly delocalized, see section VII). Applying this assumption to eq 23 then yields

$$\begin{aligned} \langle \Lambda_{\alpha j, \alpha k}(t) \Lambda_{\beta m, \beta n} \rangle &= \left[ \sum_{l=1}^{n_1} q_{l:\alpha j, \alpha k} q_{l:\beta m, \beta n} \right] C_{FF}(t) \\ &\equiv A_{\alpha j, \alpha k; \beta m, \beta n} C_{FF}(t) \end{aligned} \quad (25)$$

The coefficients  $\{A_{\alpha j, \alpha k; \beta m, \beta n}\}$  can then be calculated explicitly provided that the eigenfunctions of the anharmonic vibrational Hamiltonian are known. The spectral density that corresponds to  $C_{FF}(t)$  can be obtained as

$$\begin{aligned} \int_0^\infty d\tau e^{i\omega\tau} C_{FF}(\tau) &\approx \text{Re} \int_0^\infty d\tau e^{i\omega\tau} C_{FF}(\tau) \\ &= \frac{1}{2} \int_{-\infty}^\infty d\tau e^{i\omega\tau} C_{FF}(\tau) \\ &\equiv \frac{1}{2} \tilde{C}_{FF}(\omega) = \frac{2}{1 + e^{-\beta\hbar\omega}} \tilde{C}_{FF}^S(\omega) \\ &\approx \frac{2}{1 + e^{-\beta\hbar\omega}} \tilde{C}_{FF}^{\text{cl}}(\omega) \end{aligned} \quad (26)$$

The first approximation,  $\int_0^\infty d\tau e^{i\omega\tau} C_{FF}(\tau) \approx \text{Re} \int_0^\infty d\tau e^{i\omega\tau} C_{FF}(\tau)$ , is based on assuming that the imaginary part can be neglected; the fourth equality,  $1/2 \tilde{C}_{FF}(\omega) = (2/(1 + e^{-\beta\hbar\omega})) \tilde{C}_{FF}^S(\omega)$ , is based

on an identity that relates the Fourier transform of  $C_{FF}(\tau)$ , i.e.,  $\tilde{C}_{FF}(\omega)$ , with that of  $ReC_{FF}(\tau)$ , i.e.,  $\tilde{C}_{FF}^S(\omega)$ ; the fifth equality is based on assuming that the real part of the force correlation function,  $ReC_{FF}(\tau)$ , can be approximated by the classical force correlation function,  $C_{FF}^{cl}(\tau)$ . This procedure assures that detailed balance is satisfied within the band

$$\frac{\tilde{C}_{FF}(\omega)}{\tilde{C}_{FF}(-\omega)} = \frac{1 + e^{\beta\hbar\omega}}{1 + e^{-\beta\hbar\omega}} = e^{\beta\hbar\omega} \quad (27)$$

Although the above treatment is equivalent to employing the so-called harmonic quantum correction factor, quantum corrections are expected to be minimal in light of the fact that our model only accounts for energy relaxation between states that belong to the same manifold, and therefore involve transition frequencies that are smaller than  $k_B T/\hbar$ . Under these circumstances, other quantum correction factors would be expected to yield similar results. Thus, the only reason for including the harmonic quantum correction factor (or any other quantum correction factor for that matter) is to preserve detailed balance, rather than accounting for extensive quantum corrections beyond that.<sup>68</sup>

Substituting eqs 25 and 26 into eq 11 then yields the following general expression for the relaxation coefficients that appear in the QMEs, eqs 8–10

$$\begin{aligned} \Gamma_{\alpha_j, \alpha_k; \beta_m, \beta_n}(\omega) &= \frac{2A_{\alpha_j, \alpha_k; \beta_m, \beta_n}}{\hbar^2} \frac{1}{1 + e^{-\beta\hbar\omega}} \tilde{C}_{FF}^{cl}(\omega) \\ &\approx \frac{2A_{\alpha_j, \alpha_k; \beta_m, \beta_n}}{\hbar^2} \frac{1}{1 + e^{-\beta\hbar\omega}} \tilde{C}_{FF}^{cl}(0) \end{aligned} \quad (28)$$

The last approximation in eq 28 is based on the fact that  $\tilde{C}_{FF}^{cl}(\omega)$  is typically observed to remain within the relatively narrow range of intraband transition frequencies considered here. Thus, we are left with a single parameter, namely  $\tilde{C}_{FF}^{cl}(0)$ , which can either be obtained from molecular dynamics simulations or by fitting to experiment.

Further insight can be obtained by considering the expressions for some of the relaxation coefficients that can be obtained based on eq 28. For example, the population relaxation rate constants can be shown to be given by

$$\begin{aligned} k_{\alpha_m - \alpha_j} &= 2Re[\Gamma_{\alpha_j, \alpha_m; \alpha_m, \alpha_j}(\omega_{\alpha_j, \alpha_m})] \\ &\approx \frac{4}{\hbar^2} \sum_{l=1}^{n_1} q_{l; \alpha_j, \alpha_m}^2 \frac{1}{1 + e^{-\beta\hbar\omega_{\alpha_j, \alpha_m}}} \tilde{C}_{FF}^{cl}(0) \end{aligned} \quad (29)$$

and are seen to depend solely on the off-diagonal matrix elements of  $q_l$ . In practice, the latter are found to be small compared to the diagonal ones, which is consistent with the observation that population relaxation is slower compared to pure dephasing despite of the fact that  $\beta\hbar\omega_{\alpha_j, \alpha_m} < 1$ .

Next, consider the interband and intraband pure dephasing rate constants

$$\begin{aligned} \left(\frac{1}{T_2^*}\right)_{\alpha_j, \beta_k} &\equiv \Gamma_{\alpha_j, \alpha_j; \alpha_j, \alpha_j}(0) + \Gamma_{\beta_k, \beta_k; \beta_k, \beta_k}^*(0) \\ &- \Gamma_{\beta_k, \beta_k; \alpha_j, \alpha_j}(0) - \Gamma_{\alpha_j, \alpha_j; \beta_k, \beta_k}^*(0) \approx \frac{1}{\hbar^2} \sum_{l=1}^{n_1} [q_{l; \alpha_j, \alpha_j} \\ &- q_{l; \beta_k, \beta_k}]^2 \tilde{C}_{FF}^{cl}(0) \end{aligned} \quad (30)$$

$$\begin{aligned} \left(\frac{1}{T_2^*}\right)_{\alpha_j, \alpha_k} &= \Gamma_{\alpha_j, \alpha_j; \alpha_j, \alpha_j}(0) + \Gamma_{\alpha_k, \alpha_k; \alpha_k, \alpha_k}^*(0) \\ &- \Gamma_{\alpha_k, \alpha_k; \alpha_j, \alpha_j}(0) - \Gamma_{\alpha_j, \alpha_j; \alpha_k, \alpha_k}^*(0) \\ &= \frac{1}{\hbar^2} \sum_{l=1}^{n_1} [q_{l; \alpha_j, \alpha_j} - q_{l; \alpha_k, \alpha_k}]^2 \tilde{C}_{FF}^{cl}(0) \end{aligned} \quad (31)$$

It should be noted that the interband pure dephasing rate constant relies on the difference between the diagonal elements of  $q_l$  in different bands, thereby making it rather sensitive to anharmonicities. In contrast, the intraband pure dephasing rate constant rely on the difference between the diagonal elements of  $q_l$  within the same band, and can therefore be expected to be significantly slower.

The interband and intraband coherence transfer terms and the population-coherence transfer terms can be shown to involve both diagonal and off-diagonal matrix elements of  $q_l$ . More specifically, the matrix elements appear as pair products where either both members in the pair are off-diagonal or one is diagonal and one is not. In practice, we have observed that the diagonal elements are larger. Thus, a reasonable approximation can be based on neglecting the terms that involve two off-diagonals

$$\begin{aligned} \left[\frac{d}{dt} \sigma_{\alpha_j, \beta_k}(t)\right]_{\text{coh} - \text{coh}} &\approx \\ &- \frac{2\tilde{C}_{FF}^{cl}(0)}{\hbar^2} \left\{ \sum_{m \neq j} \sum_{l=1}^{n_1} \left[ \frac{1}{1 + e^{-\beta\hbar\omega_{\alpha_m, \alpha_j}}} q_{l; \alpha_j, \alpha_j} q_{l; \alpha_j, \alpha_m} \right. \right. \\ &+ \left. \frac{1}{2} q_{l; \alpha_j, \alpha_m} q_{l; \alpha_m, \alpha_m} \right] \sigma_{\alpha_m, \beta_k}(t) \\ &+ \sum_{m \neq k} \sum_{l=1}^{n_1} \left[ \frac{1}{1 + e^{-\beta\hbar\omega_{\beta_m, \beta_k}}} q_{l; \beta_k, \beta_k} q_{l; \beta_k, \beta_m} \right. \\ &+ \left. \left. \frac{1}{2} q_{l; \beta_k, \beta_m} q_{l; \beta_m, \beta_m} \right] \sigma_{\alpha_j, \beta_m}(t) \right\} \end{aligned} \quad (32)$$

$$\begin{aligned} \left[\frac{d}{dt} \sigma_{\alpha_j, \alpha_k}(t)\right]_{\text{coh} - \text{coh}} &\approx \\ &- \frac{1}{\hbar^2} \tilde{C}_{FF}^{cl}(0) \sum_{m \neq (j, k)} \sum_{l=1}^{n_1} [q_{l; \alpha_j, \alpha_m} q_{l; \alpha_m, \alpha_m} \sigma_{\alpha_m, \alpha_k}(t) \\ &+ q_{l; \alpha_k, \alpha_m} q_{l; \alpha_m, \alpha_m} \sigma_{\alpha_j, \alpha_m}(t)] \end{aligned} \quad (33)$$

$$\begin{aligned} \left[\frac{d}{dt} \sigma_{\alpha_j, \alpha_k}(t)\right]_{\text{coh} - \text{pop}} &\approx \\ &- \frac{2\tilde{C}_{FF}^{cl}(0)}{\hbar^2} \left\{ \left[ \frac{1}{1 + e^{-\beta\hbar\omega_{\alpha_k, \alpha_j}}} q_{l; \alpha_j, \alpha_j} q_{l; \alpha_j, \alpha_k} \right. \right. \\ &+ \left. \frac{1}{2} q_{l; \alpha_j, \alpha_k} q_{l; \alpha_k, \alpha_k} \right] \sigma_{\alpha_k, \alpha_k}(t) \\ &+ \left[ \frac{1}{2} q_{l; \alpha_k, \alpha_j} q_{l; \alpha_j, \alpha_j} + \frac{1}{1 + e^{-\beta\hbar\omega_{\alpha_j, \alpha_k}}} q_{l; \alpha_k, \alpha_k} q_{l; \alpha_k, \alpha_j} \right] \sigma_{\alpha_j, \alpha_j}(t) \left. \right\} \end{aligned} \quad (34)$$

## IV. FIELD-MATTER INTERACTION

The interaction of the system with the laser is treated perturbatively. The interaction Hamiltonian is given by

$$W(t) = -\vec{V} \cdot \vec{E}(t) \cos[\omega t - \vec{k} \cdot \vec{r}] \quad (35)$$

where  $\vec{E}(t)$ ,  $\vec{k}$ , and  $\omega$  are the envelope, wave vector and leading frequency of the driving field and  $V$  is the dipole moment vector operator. It is assumed that the bandwidth of the laser overlaps with the fundamental transition (ground state to the first-excited band) and overtone transition (first-excited band to the second-excited band). Thus, within the rotating wave approximation (RWA)<sup>69–71</sup>

$$\begin{aligned} \hat{W}(t) = & -\frac{\hbar}{2} e^{i\omega t - i\vec{k} \cdot \vec{r}} \left[ \sum_{j=0}^{n_1-1} \chi_{00,1j}(t) |00\rangle\langle 1j| \right. \\ & \left. + \sum_{j=0}^{n_1-1} \sum_{k=0}^{n_2-1} \chi_{1j,2k}(t) |1j\rangle\langle 2k| \right] \\ & -\frac{\hbar}{2} e^{-i\omega t + i\vec{k} \cdot \vec{r}} \left[ \sum_{j=0}^{n_1-1} \chi_{1j,00}(t) |1j\rangle\langle 00| \right. \\ & \left. + \sum_{j=0}^{n_1-1} \sum_{k=0}^{n_2-1} \chi_{2k,1j}(t) |2k\rangle\langle 1j| \right] \end{aligned} \quad (36)$$

Here

$$\begin{aligned} \hbar\chi_{\alpha j, \beta k}(t) &= \vec{V}_{\alpha j, \beta k} \cdot \vec{E}(t) = \sum_b V_{\alpha j, \beta k, b} E_b(t) \\ &= \sum_b \hbar\chi_{\alpha j, \beta k, b}(t) \end{aligned} \quad (37)$$

where  $\{\vec{V}_{\alpha i \beta j} = (V_{\alpha i \beta j, x}, V_{\alpha i \beta j, y}, V_{\alpha i \beta j, z})\}$  are the transition dipole moments which are assumed to be constant vectors (the Condon approximation). Dark transitions can be included by setting the corresponding transition dipole moments to zero,  $\vec{V}_{\alpha i \beta j} = 0$ .

In order to eliminate rapidly oscillating terms, it is desirable to calculate the system's optical response in the *rotating frame*. To this end, we define the density operator in the rotating frame picture as follows:

$$\tilde{\sigma}(t) = e^{iH_{\text{rot}}t/\hbar} \hat{\sigma}(t) e^{-iH_{\text{rot}}t/\hbar} \quad (38)$$

where

$$\hat{H}_{\text{rot}} = \hbar\omega \sum_{j=0}^{n_1-1} |1j\rangle\langle 1j| + 2\hbar\omega \sum_{j=0}^{n_2-1} |2j\rangle\langle 2j| \quad (39)$$

As a result:

$$\sigma_{\alpha j, \beta k}(t) = e^{-i\omega_{\alpha\beta}^{\text{rot}}t} \tilde{\sigma}_{\alpha j, \beta k}(t) \Leftrightarrow \tilde{\sigma}_{\alpha j, \beta k}(t) = e^{i\omega_{\alpha\beta}^{\text{rot}}t} \sigma_{\alpha j, \beta k}(t) \quad (40)$$

where  $\omega_{\alpha\alpha}^{\text{rot}} = 0$ ,  $\omega_{10}^{\text{rot}} = -\omega_{01}^{\text{rot}} = \omega_{21}^{\text{rot}} = -\omega_{12}^{\text{rot}} = \omega$ ,  $\omega_{20}^{\text{rot}} = -\omega_{02}^{\text{rot}} = 2\omega$ . It is important to note that the populations and intraband coherences are invariant to the transformation to the rotating frame and that only interband coherences ( $\alpha \neq \beta$ ) change as a result of it.

Next we consider the effect on the system of an interaction with a light pulse which is short on the time scale of the system relaxation. Under these conditions, relaxation dynamics can be neglected during the period of the pulse. Assuming for the sake of

simplicity, that the pulse has a square profile, such that

$$\chi_{\alpha j, \beta k}(t) = \begin{cases} \chi_{\alpha j, \beta k} & \text{during pulse} \\ 0 & \text{otherwise} \end{cases} \quad (41)$$

one can describe the dynamics during the short time period when the pulse is on by equation of motion in the rotating frame

$$\frac{d}{dt} \tilde{\sigma}(t) = -\frac{i}{\hbar} [\tilde{H}, \tilde{\sigma}(t)] \quad (42)$$

where

$$\begin{aligned} \tilde{H} = & \sum_{j=0}^{n_1-1} \Delta_{1j} |1j\rangle\langle 1j| + \sum_{j=0}^{n_2-1} \Delta_{2j} |2j\rangle\langle 2j| \\ & -\frac{\hbar}{2} e^{-i\vec{k} \cdot \vec{r}} \left[ \sum_{j=0}^{n_1-1} \chi_{00,1j} |00\rangle\langle 1j| + \sum_{j=0}^{n_1-1} \sum_{k=0}^{n_2-1} \chi_{1j,2k} |1j\rangle\langle 2k| \right] \\ & -\frac{\hbar}{2} e^{i\vec{k} \cdot \vec{r}} \left[ \sum_{j=0}^{n_1-1} \chi_{1j,00} |1j\rangle\langle 00| + \sum_{j=0}^{n_1-1} \sum_{k=0}^{n_2-1} \chi_{2k,1j} |2k\rangle\langle 1j| \right] \end{aligned} \quad (43)$$

Here,  $\Delta_{\alpha j} = \omega_{\alpha 0} + \varepsilon_{\alpha j} - \alpha\omega$  is the detuning. Assuming resonance,  $|\Delta_{\alpha j}| \ll |\chi_{\alpha j, \beta k}|$ , the rotating-frame interaction Hamiltonian can be further simplified to become

$$\begin{aligned} \tilde{H} = & -\frac{\hbar}{2} e^{-i\vec{k} \cdot \vec{r}} \left[ \sum_{j=0}^{n_1-1} \chi_{00,1j} |00\rangle\langle 1j| \right. \\ & \left. + \sum_{j=0}^{n_1-1} \sum_{k=0}^{n_2-1} \chi_{1j,2k} |1j\rangle\langle 2k| \right] \\ & -\frac{\hbar}{2} e^{i\vec{k} \cdot \vec{r}} \left[ \sum_{j=0}^{n_1-1} \chi_{1j,00} |1j\rangle\langle 00| \right. \\ & \left. + \sum_{j=0}^{n_1-1} \sum_{k=0}^{n_2-1} \chi_{2k,1j} |2k\rangle\langle 1j| \right] \end{aligned} \quad (44)$$

Furthermore, in the limit of weak field-matter interaction, one can treat the latter perturbatively, so that the evolution (in the rotating frame) during a pulse of length  $\tau_p$  is given by

$$\begin{aligned} \exp\left[-\frac{i}{\hbar} \tilde{H} \tau_p\right] &= 1 - \frac{i}{\hbar} \tilde{H} \tau_p \\ &= 1 + \frac{i}{2} e^{-i\vec{k} \cdot \vec{r}} \hat{\Omega}^- + \frac{i}{2} e^{i\vec{k} \cdot \vec{r}} \hat{\Omega}^+ \end{aligned} \quad (45)$$

where

$$\begin{aligned} \hat{\Omega}^- &= \sum_b \hat{\Omega}_b^- = \tau_p \sum_b \left[ \sum_{j=0}^{n_1-1} \chi_{00,1j,b} |00\rangle\langle 1j| \right. \\ & \left. + \sum_{j=0}^{n_1-1} \sum_{k=0}^{n_2-1} \chi_{1j,2k,b} |1j\rangle\langle 2k| \right] \\ \hat{\Omega}^+ &= \sum_b \hat{\Omega}_b^+ = \tau_p \sum_b \left[ \sum_{j=0}^{n_1-1} \chi_{1j,00,b} |1j\rangle\langle 00| \right. \\ & \left. + \sum_{j=0}^{n_1-1} \sum_{k=0}^{n_2-1} \chi_{2k,1j,b} |2k\rangle\langle 1j| \right] \end{aligned} \quad (46)$$

Finally, we note that the field-free evolution in the rotating frame can be described by eqs 8–10, except for the fact that  $\omega_{\alpha_j, \beta k}$  needs to be replaced by

$$\Delta_{\alpha_j, \beta k} = \omega_{\alpha_j, \beta k} - \omega_{\alpha\beta}^{\text{rot}} \quad (47)$$

## V. REPHASING AND NONREPHASING SIGNALS

Let  $\mathbf{k}_\alpha, \mathbf{k}_\beta, \mathbf{k}_\gamma$  be the wave vectors of the first ( $\alpha$ ), second ( $\beta$ ), and third ( $\gamma$ ) pulses, respectively. Let the time intervals between pulses  $\alpha$  and  $\beta$  be  $t_1$ , and between pulses  $\beta$  and  $\gamma$  be  $t_2$ . Let  $t_3$  be the time interval between pulse  $\gamma$  and detection. The rephasing and nonrephasing signals are defined as the signal fields measured in the directions  $\mathbf{k}_r = -\mathbf{k}_\alpha + \mathbf{k}_\beta + \mathbf{k}_\gamma$  and  $\mathbf{k}_{nr} = \mathbf{k}_\alpha - \mathbf{k}_\beta + \mathbf{k}_\gamma$ , respectively. These signals can then be calculated based on the algorithm described below.

We start out with the system at equilibrium ( $t = 0_-$  implies prior to the first pulse while  $t = 0_+$  implies right after the first pulse)

$$\tilde{\sigma}(0_-) = |00\rangle\langle 00| \quad (48)$$

The interaction with the  $b_\alpha$  component  $b_\alpha = [b_{\alpha,x}, b_{\alpha,y}, b_{\alpha,z}]$  of the first pulse (laser pulse  $\alpha$ ) can then be described by

$$\begin{aligned} \tilde{\sigma}(0_+) = & \left[ 1 + \frac{i}{2} e^{-i\mathbf{k}_\alpha \cdot \mathbf{r}} \hat{\Omega}_{b_\alpha}^- \right. \\ & \left. + \frac{i}{2} e^{i\mathbf{k}_\alpha \cdot \mathbf{r}} \hat{\Omega}_{b_\alpha}^+ \right] \tilde{\sigma}(0_-) \left[ 1 - \frac{i}{2} e^{-i\mathbf{k}_\alpha \cdot \mathbf{r}} \hat{\Omega}_{b_\alpha}^- - \frac{i}{2} e^{i\mathbf{k}_\alpha \cdot \mathbf{r}} \hat{\Omega}_{b_\alpha}^+ \right] \end{aligned} \quad (49)$$

This product can be broken into 9 terms. However, we are only interested in the terms that contribute to the rephasing and nonrephasing signals. Since the *rephasing signal* is along the wave vector  $\mathbf{k}_r = -\mathbf{k}_\alpha + \mathbf{k}_\beta + \mathbf{k}_\gamma$ , only the following two terms that go as  $e^{-i\mathbf{k}_\alpha \cdot \mathbf{r}}$ , out of the nine, contribute to it

$$\tilde{\sigma}(0_+) \xrightarrow{\text{rephasing}} \frac{i}{2} e^{-i\mathbf{k}_\alpha \cdot \mathbf{r}} [\hat{\Omega}_{b_\alpha}^- \tilde{\sigma}(0_-) - \tilde{\sigma}(0_-) \hat{\Omega}_{b_\alpha}^-] \quad (50)$$

Similarly, for the *nonrephasing signal*, which is along  $\mathbf{k}_{nr} = \mathbf{k}_\alpha - \mathbf{k}_\beta + \mathbf{k}_\gamma$ , only the following two terms that go as  $e^{i\mathbf{k}_\alpha \cdot \mathbf{r}}$  contribute to it

$$\tilde{\sigma}(0_+) \xrightarrow{\text{nonrephasing}} \frac{i}{2} e^{i\mathbf{k}_\alpha \cdot \mathbf{r}} [\hat{\Omega}_{b_\alpha}^+ \tilde{\sigma}(0_-) - \tilde{\sigma}(0_-) \hat{\Omega}_{b_\alpha}^+] \quad (51)$$

In the next step, the field-free evolution between pulses  $\alpha$  and  $\beta$  is obtained by solving the QMEs, eqs 8–10, in the rotating frame. More specifically, by writing the QME for  $\tilde{\sigma}_{\alpha_j, \beta k}(t)$  in the following way

$$\frac{d}{dt} \tilde{\sigma}_{\alpha_j, \beta k}(t) = -i\Delta_{\alpha_j, \beta k} \tilde{\sigma}_{\alpha_j, \beta k}(t) - \sum_{\gamma m, \delta n} \mathbf{R}_{\alpha_j, \beta k; \gamma m, \delta n} \tilde{\sigma}_{\gamma m, \delta n}(t) \quad (52)$$

where  $\{\mathbf{R}_{\alpha_j, \beta k; \gamma m, \delta n}\}$  stand for the relaxation coefficients given explicitly in eqs 8–10, it can be easily shown that

$$\tilde{\sigma}(t_{1-}) = \exp(-i\Delta t_1) \exp(-\mathbf{R}t_1) \tilde{\sigma}(0_+) \quad (53)$$

Here,  $\Delta$  is the diagonal matrix detuning matrix

$$\Delta = \begin{pmatrix} 0 & 0 & 0 & \cdots \\ 0 & \Delta_{10,00} & 0 & \cdots \\ 0 & 0 & \Delta_{11,00} & \cdots \\ \vdots & \vdots & \vdots & \ddots \end{pmatrix} \quad (54)$$

and  $\exp(-\mathbf{R}t_1)$  can be obtained by numerical diagonalization of the  $\mathbf{R}$  matrix.

The interaction with the  $b_\beta$  component of the second pulse is treated similarly to that of the first pulse. In the case of rephasing ( $\mathbf{k}_r = -\mathbf{k}_\alpha + \mathbf{k}_\beta + \mathbf{k}_\gamma$ ), only the two terms that go as  $e^{i\mathbf{k}_\beta \cdot \mathbf{r}}$  contribute

$$\tilde{\sigma}(t_{1+}) \xrightarrow{\text{rephasing}} \frac{i}{2} e^{i\mathbf{k}_\beta \cdot \mathbf{r}} [\hat{\Omega}_{b_\beta}^+ \tilde{\sigma}(t_1) - \tilde{\sigma}(t_1) \hat{\Omega}_{b_\beta}^+] \quad (55)$$

Similarly, for the *nonrephasing signal* ( $\mathbf{k}_{nr} = \mathbf{k}_\alpha - \mathbf{k}_\beta + \mathbf{k}_\gamma$ ) only the two terms that go as  $e^{-i\mathbf{k}_\beta \cdot \mathbf{r}}$  contribute

$$\tilde{\sigma}(t_{1+}) \xrightarrow{\text{nonrephasing}} \frac{i}{2} e^{-i\mathbf{k}_\beta \cdot \mathbf{r}} [\hat{\Omega}_{b_\beta}^- \tilde{\sigma}(t_{1-}) - \tilde{\sigma}(t_{1-}) \hat{\Omega}_{b_\beta}^-] \quad (56)$$

The field-free time evolution between pulses  $\beta$  and  $\gamma$  is then obtained similarly to that between pulses  $\alpha$  and  $\beta$

$$\tilde{\sigma}(t_1 + t_{2-}) = \exp(-i\Delta t_2) \exp(-\mathbf{R}t_2) \tilde{\sigma}(t_{1+}) \quad (57)$$

This is followed by the interaction with the  $b_\gamma$  component of the third pulse which is treated similarly to that of the first and second pulses. In this case, both rephasing ( $\mathbf{k}_r = -\mathbf{k}_\alpha + \mathbf{k}_\beta + \mathbf{k}_\gamma$ ) and nonrephasing ( $\mathbf{k}_{nr} = \mathbf{k}_\alpha - \mathbf{k}_\beta + \mathbf{k}_\gamma$ ) signals go as  $e^{i\mathbf{k}_\gamma \cdot \mathbf{r}}$ , so that the following two terms contribute:

$$\begin{aligned} \tilde{\sigma}(t_1 + t_{2+}) \xrightarrow[\text{nonrephasing}]{\text{rephasing}} & \frac{i}{2} e^{i\mathbf{k}_\gamma \cdot \mathbf{r}} [\hat{\Omega}_{b_\gamma}^+ \tilde{\sigma}(t_1 + t_{2-}) \\ & - \tilde{\sigma}(t_1 + t_{2-}) \hat{\Omega}_{b_\gamma}^+] \end{aligned} \quad (58)$$

Finally, heterodyne detection of the signal with polarization along  $b_\delta$ , corresponds to measuring the following expectation value:

$$\begin{aligned} \langle \hat{W}_{b_\delta} \rangle(t_1 + t_2 + t_3) &= \text{Tr}[\hat{\sigma}(t_1 + t_2 + t_3) \hat{W}_{b_\delta}] \\ &= \text{Tr}[e^{-iH_{\text{rot}}(t_1 + t_2 + t_3)/\hbar} \tilde{\sigma}(t_1 + t_2 \\ &+ t_3) e^{iH_{\text{rot}}(t_1 + t_2 + t_3)/\hbar} \hat{W}_{b_\delta}] = \text{Tr}[\tilde{\sigma}(t_1 + t_2 \\ &+ t_3) e^{iH_{\text{rot}}(t_1 + t_2 + t_3)/\hbar} \hat{W}_{b_\delta} e^{-iH_{\text{rot}}(t_1 + t_2 + t_3)/\hbar}] \\ &\propto \left[ \sum_{j=0}^{n_1-1} V_{00,1j,b_\delta} \tilde{\sigma}_{1j,00}(t_1 + t_2 + t_3) \right. \\ &\left. + \sum_{j=0}^{n_1-1} \sum_{k=0}^{n_2-1} V_{1j,2k,b_\delta} \tilde{\sigma}_{2k,1j}(t_1 + t_2 + t_3) \right] \end{aligned} \quad (59)$$

Steps 1–8 need to be repeated for different values of  $(t_1, t_2, t_3)$  as well as for the  $3^4 = 81$  possible tensor elements and

**Table 1. Experimental Transition Frequencies for the Ground-to-First-Manifold Transitions of Mn<sub>2</sub>(CO)<sub>10</sub> Obtained from (a) Infrared Absorption<sup>35</sup> and (b) Raman Scattering<sup>75</sup> in Nonpolar Solvents, along with the Anharmonicities for the Infrared Active States (Bold) Obtained from Transient Infrared Absorption Experiments<sup>35</sup>**

mode	experiment	
	$\omega_{1j} + \varepsilon_{1j}$ (cm <sup>-1</sup> )	$\varepsilon_{2j}$ (cm <sup>-1</sup> )
1	1981 <sup>a</sup>	
2	1981 <sup>a</sup>	
3	1983 <sup>b</sup>	-11
4	1997 <sup>a</sup>	
5	2014 <sup>b</sup>	-13
6	2014 <sup>b</sup>	-13
7	2024 <sup>a</sup>	
8	2024 <sup>a</sup>	
9	2044 <sup>b</sup>	-15
10	2116 <sup>a</sup>	

orientational averaging need to be performed in order to get the lab-frame spectrum of one's choice (XXXX, XYXY, etc).

## VI. AB INITIO CALCULATION OF THE MODEL PARAMETERS

The required input parameters include the transition energies and dipole moments, the normal-mode coordinate displacement matrix elements, the classical force–force time correlation functions, and the laser frequency and polarization. Aside from the choice of electronic structure method and MD force fields, our approach is free of adjustable phenomenological parameters. Below we describe how each of these inputs was obtained for Mn<sub>2</sub>(CO)<sub>10</sub>.

The fundamental transition frequencies  $\omega_{1j}$  (eq 2, Table 1) were obtained from infrared absorption and Raman scattering experiments of Mn<sub>2</sub>(CO)<sub>10</sub> in nonpolar solvents. We chose to use the experimental frequencies so as to compare the results directly with experiment (see below). Overtone and combination-band anharmonicities ( $\varepsilon_{2j}$ ) are set to 10 cm<sup>-1</sup>, a value that agrees well with the 2DIR experimental data for transitions between IR active states. Since the modes are highly delocalized, we expect the anharmonicities of the dark states to remain similar to those of the IR active ones. Alternatively, second-order vibrational perturbation theory (VPT2) can be used to obtain the transition frequencies for the first- and second-manifold states. We have recently shown that VPT2 gives excellent agreement with experiment for the case Mn<sub>2</sub>(CO)<sub>10</sub> and its two photoproducts Mn<sub>2</sub>(CO)<sub>9</sub> and Mn(CO)<sub>5</sub> (see ref 35 for full details). The transition dipole moments were obtained from a harmonic analysis of Mn<sub>2</sub>(CO)<sub>10</sub> using a Hessian derived from density functional theory. Electronic structure calculations were carried out using the Becke 1986 exchange and Perdew correlation functionals (BP86)<sup>72,73</sup> combined with a LANL2DZ pseudopotential basis<sup>74</sup> on the Mn atoms and a 6-31G(d) basis on the remaining atoms. The optimization gradient convergence was set to 10<sup>-6</sup> hartree/bohr and the SCF convergences were set to 10<sup>-10</sup> hartree.

In order to obtain the  $q_{l,\alpha_j,\alpha_k}$  elements of the transport coefficients, the full anharmonic Hamiltonian for the system needs to be diagonalized. The Hamiltonian, which includes third ( $\phi_{ijk}$ ) and semidiagonal fourth order ( $\phi_{ijkk}$ ) force constants, was

obtained by finite differentiation. Briefly, the molecule was displaced along each normal mode in the positive and negative directions and a Hessian was computed for each structure; the difference between the frequencies at the equilibrium and displaced geometries is directly related to the higher order force constants. Once these force constants are known, writing the molecular Hamiltonian is straightforward

$$\hat{H} = \frac{1}{2} \sum_i \phi_{ii} (q_i^2 + p_i^2) + \frac{1}{6} \sum_{ijk} \phi_{ijk} q_i q_j q_k + \frac{1}{24} \sum_{ijkk} \phi_{ijkk} q_i q_j q_k^2 \quad (60)$$

Diagonalizing the 10-oscillator anharmonic Hamiltonian to obtain the wave functions remains computationally challenging. To converge the eigenfunctions and energies, a minimum of approximately 7 basis functions per oscillator is needed, within a ten mode system, such as in the present model, the total number of basis functions needed would be 7<sup>10</sup> or approximately 280 million functions. Although the matrices are sparse, this is beyond the memory capacity of modern computers.

In the present case we include six modes in the Hamiltonian, four IR active modes and two dark modes (Table 1 modes 2 and 8). The Hamiltonian matrix is diagonalized, and the eigenvectors are used to calculate the  $q_{l,\alpha_j,\alpha_k}$  elements to be used in calculating the transport coefficients (eq 25). We observe that the diagonal elements ( $q_{l,\alpha_j,\alpha_j}$ ) which lead to pure dephasing of the interband coherences are approximately an order of magnitude larger than the off-diagonal elements ( $q_{l,\alpha_j,\alpha_k;j \neq k}$ ) which lead to coherence transfer and population relaxation. We also observe that the elements depend mostly on the third-order force constants, as the fourth order force constants have little effect on the final value of the displacement elements.

The force–force time correlation functions were obtained from a one-nanosecond molecular dynamics simulation of Mn<sub>2</sub>CO<sub>10</sub> in cyclohexane. The general Amber force field<sup>76</sup> was used to model the solvent and a custom force field was developed for Mn<sub>2</sub>CO<sub>10</sub>.<sup>77</sup> All bonds were kept rigid using the SHAKE algorithm.<sup>78</sup> The equilibration and production trajectories were run within the Canonical ensemble (NVT) at 300 K. All MD simulations were carried out using the GROMACS 4.0.5 package of programs.<sup>79</sup> The eigenvectors of the C≡O Hamiltonian in a local-mode basis were used to project the Cartesian forces onto the normal modes of Mn<sub>2</sub>(CO)<sub>10</sub>.

The laser polarization was set to  $[x,y,z] = [1/\sqrt{3}, 1/\sqrt{3}, 1/\sqrt{3}]$  and the center laser frequency was set to 2000 cm<sup>-1</sup>. In our case the laser is assumed to have infinite spectral bandwidth; the pulse envelope can be straightforwardly implemented by modulating the transition dipole moments to include a resonance overlap term for each transition. The density matrix was propagated for 15 ps along  $t_1$  and  $t_3$  using an adaptive step-size while stepping the value of  $t_2$  from 0.1 to 40 ps in 0.1 ps steps. All of the simulations were carried out in the body-fixed molecular frame. In order to simplify and streamline the code the eight-index relaxation terms  $\Gamma_{\alpha_j,\alpha_k;\beta_m,\beta_n}$  were stored in a standard query language (SQL)-like database and the sums were done by extracting the values through database queries.

## VII. SIMULATION RESULTS: SYSTEM–BATH COUPLING

Figure 5 shows the value of the force–force correlation function at  $\tau = 0$ ,  $\tilde{C}_{FF}^{\text{cl}}(0)$ , along the four IR active normal mode coordinates of Mn<sub>2</sub>(CO)<sub>10</sub> and an average correlation function obtained from the molecular dynamics simulations. The diagonal elements along the four normal modes are similar, indicating that

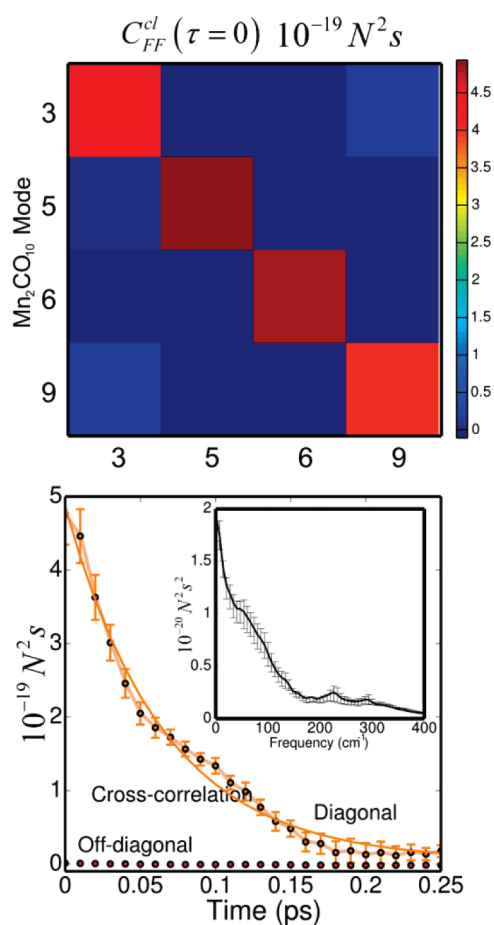


**Figure 5.** (Top) Classical force–force time-correlation functions along the four IR active modes of  $\text{Mn}_2(\text{CO})_{10}$  at  $\tau = 0$ . The diagonal terms represent the self-correlation whereas the off-diagonal terms represent the cross-correlations. (Bottom) Average diagonal and off-diagonal correlation functions corresponding to the ten modes of  $\text{Mn}_2(\text{CO})_{10}$  along with a single exponential fit to the diagonal decay. The figure shows that the force along different normal modes remains uncorrelated whereas, on average, the self-correlation decays with a time constant of  $62 \text{ fs}^{-1}$ . The inset shows the correlation function in the frequency domain obtained by Fourier transforming time-domain function from 0 to 1.5 ps. In both plots the error bars correspond to one standard deviation within the ten-mode average.

the system–solvent interactions are the same for all of the modes; this is expected since the modes are highly delocalized. Off-diagonal cross correlations are much smaller than the diagonal autocorrelations, indicating that the force fluctuations along the different modes are essentially uncorrelated. An exponential fit to the average time correlation function over the ten modes gives a decay time constant of 62 fs. The inset shows the frequency-domain behavior of the average correlation function over the  $0\text{--}135 \text{ cm}^{-1}$  range of intraband transitions. The correlation function varies within approximately a factor of 3 over this range, but for simplicity we assume that the value remains constant. Similar force fluctuations are observed for all ten normal modes regardless of IR activity.

To simplify the calculation of the relaxation coefficients, based on the molecular dynamics results we make the following two approximations: 1. The autocorrelation functions are the same for all modes and the cross correlations are zero. 2. The corresponding spectral densities are constant with respect to the frequency gaps

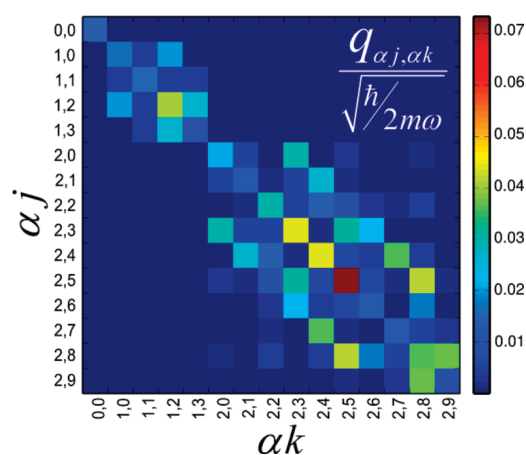


**Figure 6.** Matrix elements corresponding to the anharmonic intraband transitions. The figure shows the sum of the absolute values over all oscillators dimensionless units:  $\sum_i |q_{i\alpha_j, \alpha_k}|$ . The first block corresponds to the singly excited states, whereas the second block contains overtones and combination bands.

**Table 2. Interband Dephasing Time Constants (ps) for the Ground-to-First-Manifold Coherences and Population Relaxation Rates for the First-Manifold States Calculated for the Three Models (a–c)**

mode	interband dephasing (00,1j;00,1j)			population (1j,1j;1j,1j)		
	4 IR active	+ 1 dark	+ 2 dark	4 IR active	+ 1 dark	+ 2 dark
1981		1.6	1.0		1.3	0.7
1983	12.6	5.8	3.5	6.4	2.9	1.8
2015	5.2	5.2	2.7	104.1	71.2	2.7
2015	2.7	1.5	1.0	2.3	1.0	0.6
2024			0.6			0.4
2045	6.4	3.2	1.7	3.3	1.6	0.9

between different modes. This allows us to use the simpler form of the system–bath coupling expression as shown in eq 25.

The  $q_{\alpha_j, \alpha_k}$  elements obtained from the diagonalization of the ab initio anharmonic Hamiltonian are shown in Figure 6. As discussed above, it is presently not possible to include all ten modes, and thus six modes, four infrared active and two dark, were included in the Hamiltonian. The diagonal elements, which lead to pure dephasing, have, on average, higher amplitude than the off-diagonal elements, which lead to coherence transfer. Consequently, coherence transfer rates are on average slower than the corresponding parent dephasing rates (see eqs 9 and 10).

## VIII. DISCUSSION OF THE SIMULATION RESULTS

Three different models were devised to test the effect of dark modes on the relaxation and coherence transfer rates. The simplest model (a) contains the four IR active modes of  $\text{Mn}_2(\text{CO})_{10}$  as shown in Table 1; the second model (b) has five modes, four IR active and a single dark mode (mode 2,  $1981 \text{ cm}^{-1}$ ); the last model (c) contains four IR active and two dark modes (modes 2 and 7,  $1981$  and  $2014 \text{ cm}^{-1}$ ). The coupling between the IR active and dark modes is similar for all the dark modes, so the two modes were simply chosen as representative dark modes. It is worth mentioning that the elements of the  $q$  matrix are somewhat dependent on the specific modes included in the Hamiltonian, leading to slightly different relaxation

**Table 3. Intraband Dephasing Time Constants (ps) for the First-Manifold Coherences<sup>a</sup>**

		intraband dephasing ( $1_j, 1_k; 1_j, 1_k$ )		
		4 IR active	+ 1 dark	+ 2 dark
1981	1983		1.3	0.8
1981	2015		0.8	0.6
1981	2015		1.1	0.6
1981	2024			0.4
1981	2045		1.0	0.6
1983	1981		1.3	0.8
1983	2015	3.3	2.5	1.5
1983	2015	2.4	1.2	0.8
1983	2024			0.5
1983	2045	4.2	2.0	1.2
2015	1981		0.8	0.6
2015	1983	3.3	2.5	1.5
2015	2015	1.1	0.9	0.6
2015	2024			0.5
2015	2045	3.3	2.1	1.1
2015	1981		1.1	0.6
2015	1983	2.4	1.2	0.8
2015	2015	1.1	0.9	0.6
2015	2024			0.4
2015	2045	1.8	1.0	0.6
2024	1981			0.4
2024	1983			0.5
2024	2015			0.5
2024	2015			0.4
2024	2045			0.5
2045	1981		1.0	0.6
2045	1983	4.2	2.0	1.2
2045	2015	3.3	2.1	1.1
2045	2015	1.8	1.0	0.6
2045	2024			0.5

<sup>a</sup>The three models are described in the text. Similar to the inter-band coherences and population relaxation rates, faster dephasing is observed when a larger number of dark modes is included.

rates when different dark modes are included, but the overall trends described below are independent of the specific set of dark modes included in the simulation.

**a. Relaxation Rates and Two-Dimensional Infrared Spectra.** Table 2 shows the interband dephasing times (inverse rate constants) for coherences involving the ground and first-excited states as well as the population relaxation constants corresponding to the first manifold states, for the three model systems described above. Several observations can be made from these data. First, the relaxation rates approximately double upon addition of a single dark mode and double again upon addition of the second dark mode. For example, the dephasing times for the coherence involving mode 3 ( $1983\text{ cm}^{-1}$ ) decreases from 12.8 to 5.6 to 3.5 ps as the number of dark modes increases from zero to one to two respectively. Numerically, this arises from the increase in the number of terms included the system–bath coupling equation (eq 25) with increasing number of dark modes. The additional dark modes can thus be thought of as an effective strongly coupled “intramolecular bath” that can

accelerate the rates of dephasing for the IR active modes. Second, it can be observed that coherences and populations involving dark modes generally decay faster than those involving IR active modes. This phenomenon is observed when including different sets of dark modes but it is not clear why these modes should dephase faster since, aside from their transition dipole moments, the dark modes behave similarly to the IR active modes. Unfortunately it is difficult to test this prediction as the dark modes cannot be resonantly probed with infrared spectroscopy. Third, the dephasing and population relaxation rates for the different modes vary over a wide range. For example, the population relaxation corresponding to mode five is significantly slower than mode four in all three models. At first this may seem surprising given that the two modes share the same symmetry and are indeed degenerate. However, in the full ten-mode molecular Hamiltonian, the dark modes at  $1981$  and  $2024\text{ cm}^{-1}$  also have degenerate counterparts, we expect each degenerate mode to be coupled differently to other degenerate modes depending on the specific symmetry and the number of shared CO sites. Including one mode from each pair of dark modes in the simulation may then cause the observed differences in the dephasing rates for the degenerate IR active modes. These issues could be avoided by diagonalizing the full Hamiltonian (see the above discussion).

Intraband coherences show similar trends as interband coherences, namely the relaxation time constants become faster as additional dark modes are included in the Hamiltonian.

Table 3 shows the relaxation time constants for coherences involving states within the first manifold, these are the only intraband coherences that can be accessed with resonant third order experiments such as 2DIR spectroscopy. Addition of a single dark mode roughly doubles the dephasing time constant. This is consistent with the interpretation of the trends seen in the interband coherence rate constants. Figure 9 shows the populations, intraband coherences, and coherence–population coupling rate constants. Diagonal elements, corresponding to pure dephasing and population relaxation, remain larger than the off-diagonal elements corresponding to coherence transfer and population transfer. These results are at odds with the model of Tokmakoff and co-workers, where phenomenological fitting of the peak amplitudes along the waiting time to a Redfield model suggested that in a two-carbonyl system ( $\text{Rh}(\text{CO})_2\text{C}_5\text{H}_7\text{O}_2$ , RDC), the intraband coherence transfer rate remains very fast ( $0.35\text{ ps}^{-1}$ ) whereas the diagonal dephasing is much slower ( $10\text{ ps}^{-1}$ ).<sup>25</sup> An extra peak appearing below the diagonal in the RDC spectrum was interpreted as evidence for coherence transfer as there are no Liouville paths that lead excitation and detection at those particular frequencies in the rephasing spectrum. There is a possibility that the spectrum at zero waiting time has contributions from intramolecular vibrational redistribution (IVR) between the two first-manifold states of RDC. For example, the experimental laser pulses have a finite width of  $\sim 100\text{ fs}$ , IVR could thus give rise to the extra peak even at “zero” time delay. Using the  $3\text{ ps}^{-1}$  IVR rate reported in the paper, we should expect 3.2% of the excitation being transferred within the first 100 fs; thus pathways involving IVR between the two one-quantum states should not be discarded, even at zero waiting time. These effects could make the extracted coherence transfer rates appear somewhat faster than their actual values.

Figures 7 and 8 show the simulated and experimental 2DIR spectra  $\text{Mn}_2(\text{CO})_{10}$  respectively. Overall the simulations are in good agreement with experiment; the additional peaks observed in the experimental spectrum (i.e., peak 8) are due to naturally

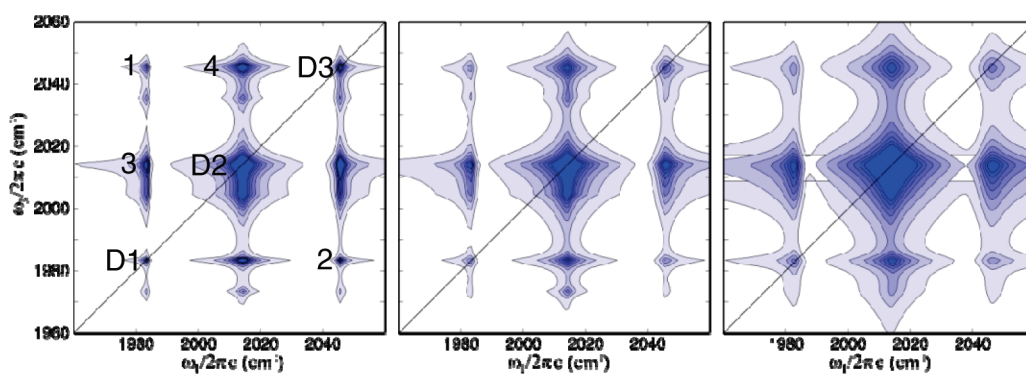


**Figure 7.** Absolute value rephasing spectra of  $\text{Mn}_2(\text{CO})_{10}$  calculated using three different models: four IR active modes (left); five modes, four IR active plus one dark mode (center); and six modes, four IR active plus two dark modes (right). The figure shows how the peaks become broadened as dark modes are included in the model. The peaks below the diagonal correspond to interband coherences involving the first and second manifolds during the detection time  $t_3$ . The waiting time dynamics of cross peaks labeled 1–4 are shown in Figures 10 and 11 below, and the three diagonal peaks labeled D1–D3 shown in Figure 13. See text for full details.

occurring isotopologues, containing a single  $^{13}\text{C}$ O substitution. Simulated two-dimensional spectra for the three model systems show that as extra modes are included, the 2D peaks become broadened. This is due to the faster dephasing of the interband coherences observed in models (b) and (c). In a 2D spectrum, the diagonal peaks and corresponding cross peaks involve coherences between the ground and first-manifold states during the excitation and detection times. The peaks appearing below the diagonal, and corresponding cross peaks, involve coherences between the first- and second-manifold states during the detection time. These peaks contain information about the two-quanta states, and are commonly referred to as “anharmonic” peaks. The anharmonic peaks remain broader than the fundamental peaks, indicating that first-to-second-manifold coherences dephase faster than the ground-to-first-manifold coherences. Two-quanta states exhibit greater anharmonic behavior than the one-quantum states as they sample a larger region of the anharmonic potential (see Figure 6). The different widths observed for the three diagonal peaks are due to the fact that the dephasing rates for the different modes can be quite different (see the above discussion). The corresponding cross peaks also exhibit different widths along the excitation and detection axes depending on the widths of the parent peaks.

**b. Vibrational Dynamics along the Waiting Time: Coherence Transfer and Coherence-Population Coupling.** The dynamics of the peaks along the waiting time ( $t_2$ ) are dictated by the dynamics of the populations and intraband coherences. Population transfer causes an overall decay of the peak amplitudes whereas intraband coherences account for the oscillations observed along the waiting time. In the absence of coherence transfer, rephasing and nonrephasing spectra show oscillations of the off-diagonal and diagonal peaks, respectively. In this section, we focus on the oscillations of the off-diagonal peaks present in the absolute-value rephasing spectra, as these can be directly compared to experiment.<sup>26</sup> To test the spectral signatures of particular couplings between states (coherence-coherence, coherence-population, etc.), we switch off the respective contributions by setting the particular rates in the relaxation matrix to either zero or their respective values obtained from the system–bath coupling equations.

Four cross peaks, labeled 1–4 in Figure 7, are selected for analysis of the amplitude along the waiting time. In the absence of off-diagonal coherence-coherence and coherence-population

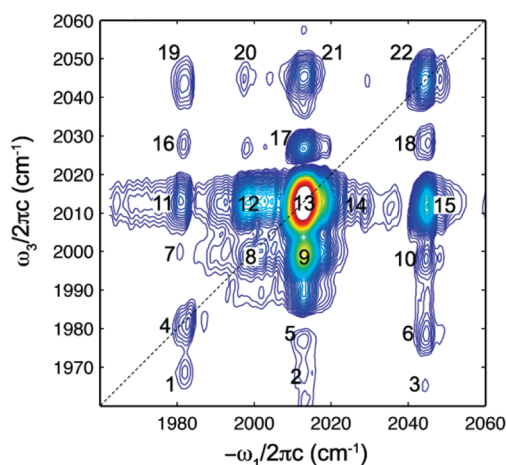


**Figure 8.** Experimental absolute-value rephasing spectrum of  $\text{Mn}_2(\text{CO})_{10}$  in cyclohexane. Adapted with permission from Nee, M.; Baiz, C.; Anna, J.; McCanne, R.; Kubarych, K. *J. Chem. Phys.* **2008**, *129*, 084503. Copyright 2008 American Institute of Physics.

couplings peaks 1 and 2 oscillate at  $62\text{ cm}^{-1}$ , the frequency corresponding to the difference between the two parent peaks ( $1983\text{--}2045\text{ cm}^{-1}$ ), and peaks 3 and 4 oscillate at a frequency of  $32\text{ cm}^{-1}$  which is similarly given by the diagonal frequencies ( $2013\text{--}2045\text{ cm}^{-1}$ ). Figures 10 and 11 show the waiting-time peak oscillations for a selected set of 2D peaks together with the corresponding frequency-domain plots. In order to focus solely on the coherence dynamics, all the population-population couplings were set to zero. Population transfer gives rise to an overall decay of the peaks but does not induce additional oscillations.

Several observations can be made from the simulation results: 1. The diagonal dephasing rate is similar for all the intraband coherences, as evidenced by the similar decay rate of the oscillations for the different peaks. Intraband dephasing rates are shown in Table 1 and discussed above. 2. Interband coherence-coherence coupling does not have any significant effect on the oscillations of the peaks along the waiting time. This is not surprising since the peak oscillations are caused by intraband coherences excited during  $t_2$ , and interband coherences are only excited during  $t_1$  and  $t_3$ . 3. Intraband coherence–coherence coupling (coherence transfer) causes peaks 1 and 2 to oscillate at

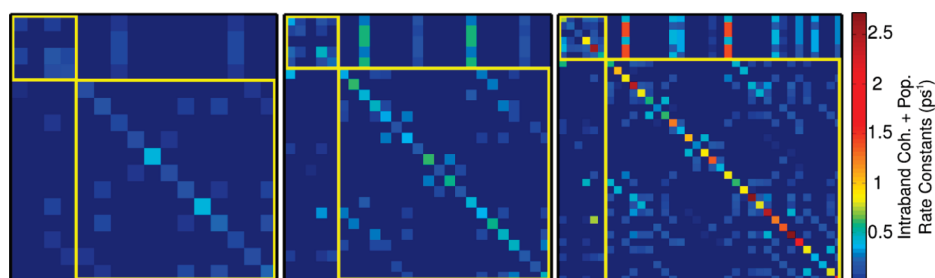


**Figure 9.** Relaxation and transfer rate constants ( $\text{ps}^{-1}$ ) for the populations (small square box in upper left corner) intraband coherences (large square box in lower right corner) along with the population-coherence coupling constants (off-diagonal blocks). The three matrices from left to right correspond to the three, four, and five mode models, respectively. To allow for direct comparison of the rates, all of the models are plotted using the same color scale shown on the right.

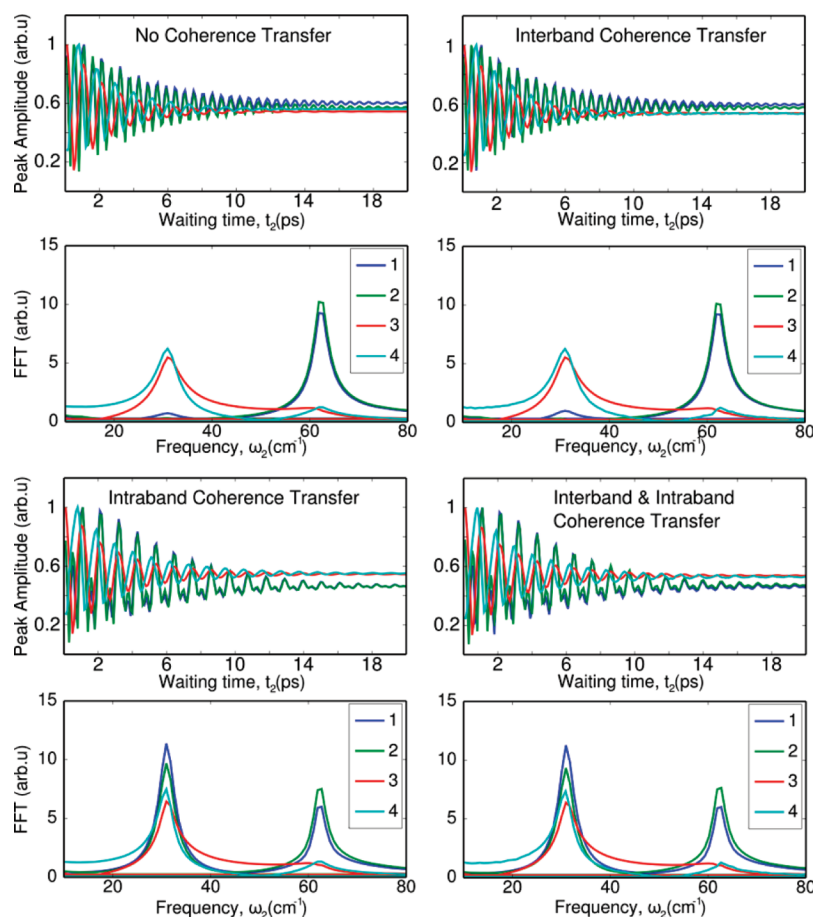


**Figure 10.** Amplitude oscillations along the waiting time corresponding to the peaks labeled 1–4 in Figure 7. All of the plots were obtained using the model which only includes the four IR active modes of  $\text{Mn}_2(\text{CO})_{10}$ . Each panel shows a plot of the peak oscillations along the waiting time ( $t_2$ , ps) with the corresponding Fourier-transforms below ( $\omega_2$ ,  $\text{cm}^{-1}$ ). Spectra were calculated at waiting times ranging from 0 to 40 ps in 0.1 ps intervals, but for clarity, the oscillations are only plotted out to 20 ps. To compare the different peak dynamics, the maximum amplitude for each peak is normalized to a value of one. Population-population coupling terms, which lead to an overall decay of the peaks, were set to zero in order to better observe the coherences. In addition to interband and intraband coherence relaxation, the four different simulations show the oscillations when including: (a) only diagonal dephasing, (b) dephasing and interband coherence–coherence coupling, (c) dephasing and intraband coherence–coherence coupling, and (d) dephasing, interband, and intraband coherence–coherence coupling as indicated within each individual plot.

two different frequencies 32 and  $62 \text{ cm}^{-1}$ , corresponding to the difference in energy between the three one-quantum levels in the system. In addition, the peaks oscillating at  $62 \text{ cm}^{-1}$  only show minimal amplitude at  $32 \text{ cm}^{-1}$ . These results are in good agreement with experiment and are discussed in detail below.

4. Interband coherence–coherence coupling has, once again, no

effect on the peak oscillations in the presence of intraband coupling. We can thus conclude that the dual-frequency oscillation of the peaks is due solely to interband coherence transfer.

5. Coherence–population coupling (Figure 11) does not have a significant effect on the oscillation frequencies of the peaks but it does affect the overall peak amplitude ratios.

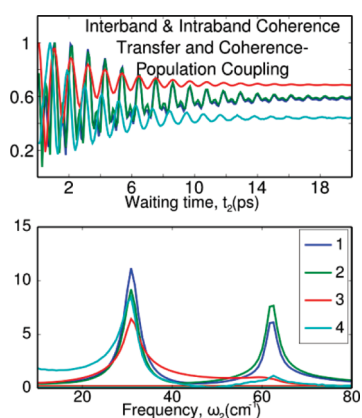


**Figure 11.** Peak amplitude oscillations along the waiting time calculated including coherence-coherence and coherence-population coupling terms. See Figure 10 for full description.

**c. Dual-Frequency Oscillations As a Signature of Coherence Transfer: A Comparison with Experiment.** To the best of our knowledge, the observation of dual-frequency oscillations of certain cross peaks in the rephasing spectra of  $\text{Mn}_2\text{-(CO)}_{10}$  represented the first direct experimental evidence for vibrational coherence transfer.<sup>26</sup> The theory and simulations presented herein are meant to shed light on the mechanism for coherence transfer in terms of the underlying molecular structure and dynamics. The present simulations are indeed found to be in semiquantitative agreement with experiment, i.e., intraband coherence transfer is seen to give rise to dual-frequency oscillations similar to those observed in the experiment. For comparison, the experimental 2DIR spectrum and corresponding peak oscillations for selected peaks are shown in Figures 8 and 12, respectively. As shown in Figure 10 and described in the previous section, in the absence of coherence transfer the cross peaks oscillate at the difference frequency of the corresponding diagonal peaks: 30 (32)  $\text{cm}^{-1}$  for coherences between the center peak (2013  $\text{cm}^{-1}$ ) the high- (low-) frequency peak, and 62  $\text{cm}^{-1}$  for coherences involving the high- and low-frequency peaks. Due to the intrinsic dephasing of the oscillations, the 30 and 32  $\text{cm}^{-1}$  coherences are indistinguishable in the frequency-domain plots. Most interestingly, in the presence of coherence transfer, the peaks that normally oscillate at 62  $\text{cm}^{-1}$  exhibit dual-frequency oscillations, but the peaks that oscillate 32  $\text{cm}^{-1}$  do not. These observations can be straightforwardly explained as follows. Since the 2013  $\text{cm}^{-1}$  mode is degenerate, there are eight possible coherences that oscillate at 30 (or 32)  $\text{cm}^{-1}$  but only two possible coherences at 62  $\text{cm}^{-1}$ . Thus, once a 62  $\text{cm}^{-1}$  intraband coherence is created, it is likely that it will be transferred to a 30 (or 32)  $\text{cm}^{-1}$  intraband coherence, whereas the reverse coherence-transfer process is much less probable. In the frequency-domain plots, the largest amplitude component appears near 30  $\text{cm}^{-1}$  for all peaks, including the peaks that normally oscillate at 62  $\text{cm}^{-1}$ . It can be observed that even in the absence of coherence transfer all oscillations show a small amplitude component at either low or high frequency. These components arise from the fact that, for absolute-value rephasing spectra, the oscillations are not simply described by a purely sinusoidal function due to the contributions from ground-state pathways (full discussion given in ref 80). Instead these  $t_2$  oscillations can be described by an equation

of the type

$$A(t_2) \propto |1 + e^{-i(\omega_{ab} + i\Gamma_{ab})t_2}| \quad (61)$$

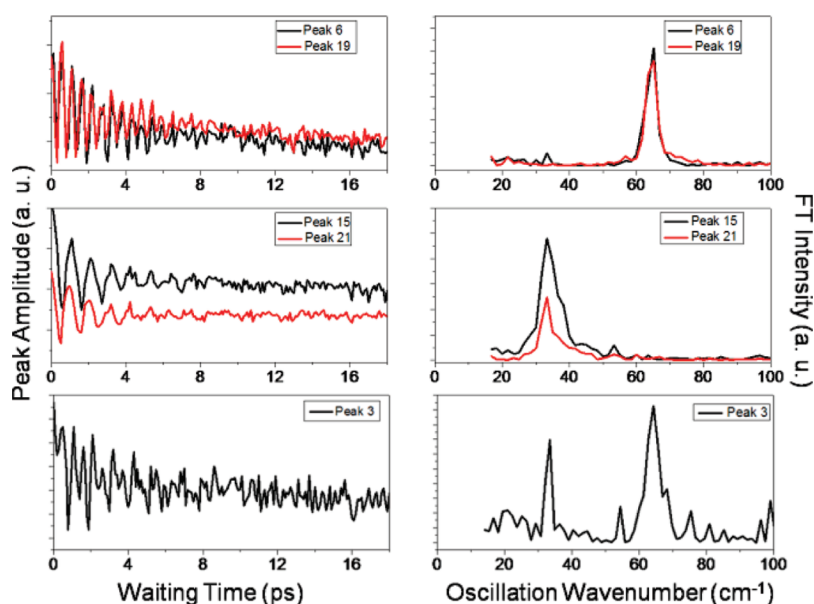
where  $\omega_{ab}$  represents the difference in frequency between levels  $a$  and  $b$  and  $\Gamma_{ab}$  is the dephasing rate constant. These observations are also consistent with the experimental results.

In addition, experimental measurements of the dephasing rates for the intraband coherences provided a direct observation of the frequency-frequency cross correlation functions for states within the same manifold. Consider the limit where the two frequencies are fully correlated. In this case, the frequency difference is constant and there should be no dephasing of the intraband coherence. In the other limit, where the frequency fluctuations remain uncorrelated, the intraband dephasing rate should be similar to the dephasing rate of the ground-to-first-manifold coherences, and thus the Fourier-transform peak widths of the oscillations should exhibit a similar width to that of the parent peaks. Indeed, the experimental data suggests that the frequency fluctuations are uncorrelated. The results are consistent with the MD simulations which showed that the force fluctuations along different modes remain uncorrelated.

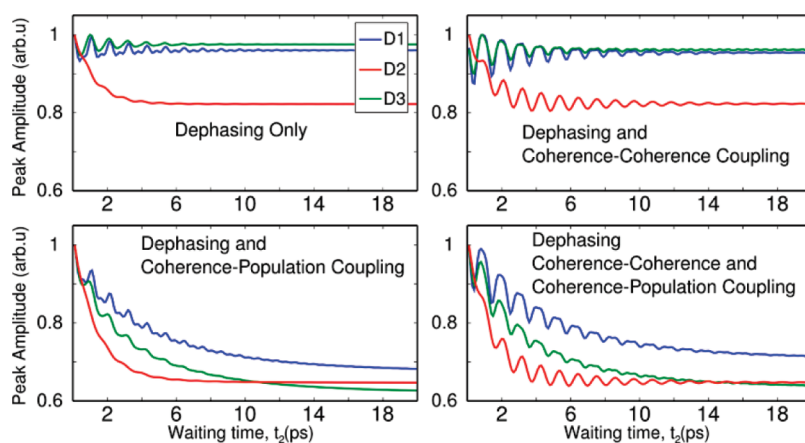
**d. Diagonal Peak Oscillations Are Induced by Coherence-Coherence Coupling.** Liouville pathways that involve intraband coherences along  $t_2$  only contribute to off-diagonal peaks in the rephasing signal. In the absence of coherence transfer or coherence-population coupling, the dynamics of the diagonal peaks as a function of the waiting time are solely dictated by the populations and therefore no oscillations should be observed. Monitoring the amplitudes of the diagonal peaks in the rephasing spectrum provides an additional test for coherence transfer and coherence-population coupling.

Figure 11 shows the amplitudes corresponding to the three diagonal peaks (D1–D3) simulated using the different relaxation models as indicated in each plot. The upper left plot is calculated using only intraband and interband dephasing. In this case there should be no oscillations observed, however there are very small dual-frequency oscillations present. The oscillations are due to a small overlap between the Lorentzian tails of the oscillating off-diagonal peaks and the diagonal peaks. In the absence of coherence transfer the diagonal peaks oscillate in phase with respect to the off-diagonal peaks, but the phase changes in the presence of coherence transfer, indicating that there are additional effects leading to the oscillations of the diagonal peaks. The lower left panel shows the dynamics in the presence of nonsecular coherence-population coupling terms. In this case the peaks decay exponentially but the oscillations remain small. We can therefore conclude that, within the present model, coherence-population couplings do not induce oscillations of the diagonal peaks but only an additional decay. Experimentally isolating the extra decay due to coherence-population coupling may be difficult as the signal contains relaxation factors from intramolecular vibrational redistribution, orientational relaxation, and vibrational energy relaxation. It is worth noting that similar to coherence transfer, some coherences are strongly coupled to populations, as shown in Figure 9. This accounts for the different decay rates observed for the three diagonal peaks.

Unlike coherence-population coupling, coherence transfer does undoubtedly induce extra oscillations of the diagonal peaks, as shown in the upper right panel of Figure 13. Naturally, coherence transfer enables new Liouville pathways that lead to coherences during the waiting time, yet contribute to diagonal peaks. Analogous to the off-diagonal peaks, the oscillation frequency remains at 30  $\text{cm}^{-1}$ , as there



**Figure 12.** Experimental peak amplitude oscillations along the waiting time with their corresponding Fourier-transforms. The labels correspond to the peaks labeled 1–22 in the experimental spectrum shown in Figure 8. The bottom panel (peak 3) shows the dual-frequency oscillations observed due to coherence-transfer. Adapted with permission from Nee, M.; Baiz, C.; Anna, J.; McCanne, R.; Kubarych, K. *J. Chem. Phys.* **2008**, *129*, 084503. Copyright 2008 American Institute of Physics.



**Figure 13.** Amplitude oscillations of the three diagonal peaks labeled D1–D3 in Figure 7. The spectra were obtained using the same model described in Figures 10 and 11. The relaxation coefficients included in each simulation are indicated within each plot.

is a larger number of coherences near this frequency (see the discussion in the previous section). Unfortunately, since the oscillation amplitudes are small, roughly 10% of the total peak amplitude in our model, they have not been observed in the experiment. Further theoretical modeling may reveal additional information regarding the coherence-coherence or coherence-population coupling contained in the phase difference between the diagonal and off-diagonal peak oscillations. In our case the phase difference between the diagonal peaks D1 and D3 and the off-diagonal peaks connecting D1 and D3 to the center diagonal peak (D2) is  $109 \pm 4^\circ$ . It remains unclear, however, how this phase difference can be interpreted in terms of an interference between different Liouville paths.

Finally, including coherence transfer and coherence-population coupling terms (Figure 13, lower right plot) shows oscillations and an overall decay of the peaks but no additional features. Thus we conclude that the two effects of coherence-coherence and coherence-population coupling are additive and may be

treated separately. From a Liouville-pathway point of view, it is not clear why oscillations are induced by coherence–coherence but not population–coherence coupling as both terms enable new pathways that ought to contribute to oscillations. However, since in our systems there are  $N[N - 1]$  coherences and  $N$  populations, from a probabilistic perspective it is more likely that a coherence will transfer to another coherence instead of to a population. It would be informative to perform similar simulations on smaller systems such as RDC, where there is only on intraband coherence and two populations within the first manifold. Similar to  $\text{Mn}_2(\text{CO})_{10}$  no diagonal oscillations of the rephasing spectra have been experimentally observed in RDC.

We would like to comment on the relationship between our findings and the recent experimental studies<sup>81,82</sup> which argued that population-coherence coupling<sup>83</sup> may contribute to efficient energy transport in photosynthetic complexes. Despite the rapid dephasing that characterizes electronic states, long-lived coherences were

observed in these systems even at ambient temperature.<sup>84</sup> In the light of these experiments, Mukamel and co-workers investigated the effect of coherence transfer and coherence–population coupling in excitonic complexes that mimic photosynthetic reaction centers.<sup>85</sup> Their model is different from ours in several respects, including the assumption of bilinear system–bath coupling to a harmonic bath and the fact that the system’s dynamics are modeled in terms of a QME of the Linblad type. In contrast to our simulations, the authors observe direct oscillations of the populations, to which they attribute the experimentally observed long-lived oscillatory behavior of the diagonal peaks as a function of the waiting time. The authors concluded that coupling between the populations and the coherences leads to longer-lived coherences, as the populations “feed” the electronic coherences. In our case coherence–coherence coupling does not lead to oscillations of the populations as these elements remain decoupled from the coherences. Including coherence–population coupling terms leads to multiexponential evolution of the population with an additional growth and decay for some elements, but not to oscillatory behavior. Furthermore, the transfer rates of coherences to populations are faster than the transfer rates from populations to coherences (Figure 9). As a result, coherences can get “trapped” into populations but not the reverse. The origin for the difference appear to lie in the different nature of the system (vibrational vs electronic), the bath (nonpolar liquid vs protein in aqueous solution), and the coupling between them. In our cases, the relative simplicity of the system allows us to trace back each and every observation to the underlying molecular dynamics and electronic structure, whereas the same is still not possible in the case of photosynthetic complexes in light of their complexity and the fact that modeling the dynamics of excited electronic states remains extremely challenging for modern electronic structure methods even for systems of modest size. The question of whether the oscillations of populations is an important phenomenon in vibrational systems remains open, but it is clear that coherence transfer can lead to oscillations of the diagonal peaks in the rephasing spectrum. We believe that future ultrafast measurements will further elucidate the complex issue of nonsecular effects, particularly in vibrational systems such as  $\text{Mn}_2(\text{CO})_{10}$  where peaks remain narrow and coherences long-lived.

## IX. CONCLUSION AND OUTLOOK

We presented a general and comprehensive theoretical and computational framework for modeling ultrafast multidimensional infrared spectra of a vibrational excitonic system in liquid solution. Using this approach we were able to provide new molecular insight into the vibrational dynamics of metal carbonyls. By disentangling the different contributions to the relaxation matrix it became possible to understand the individual signatures of coherence transfer, coherence–population coupling, and dark states on the spectra. Three different models which included, four, five, and six normal modes were explored in an effort to understand the role of dark modes on the dephasing and coherence transfer rates of our  $\text{Mn}_2(\text{CO})_{10}$  model system.

The simulation results are consistent with the experimental data and the previous interpretation of the experiment. Coherence transfer leads to dual-frequency oscillations of the cross peaks in the rephasing signal and, in a four level system with a degenerate state like the one presented here, the number of coherences at a given frequency dictates the dominant oscillation frequency for the cross peaks. The uncorrelated fluctuations of the energy levels yield similar inter- and intraband dephasing rates; thus the width of the low-frequency peaks along  $\omega_2$  are similar to the widths of the parent peaks along  $\omega_1$  and  $\omega_3$ . Coherence–population coupling was

observed to not have a significant effect on the peak dynamics, but coherence transfer was observed to lead to dual-frequency oscillations of the cross peaks as well as oscillations of the diagonal peaks. Though the amplitudes seem to remain small, given a suitable signal-to-noise ratio, these effects may be observed in future experiments.

Our approach can provide a rather rigorous theoretical framework for analyzing the vibrational dynamics of a variety of systems, and understanding the system–bath interactions in different combinations of molecules and solvents. The nice agreement of the results with experiment is encouraging. The fact that the simulations predict fine effects such as oscillations of the diagonal peaks in the rephasing spectra, provide motivation for improving the accuracy of the spectra in order to test these predictions experimentally. Importantly, since the model inputs are derived from electronic structure and molecular dynamics simulations, at least in principle, there is no need for employing phenomenological fitting parameters. Once a chemical structure and a solvent are selected, the only “free” choices are the level of electronic-structure theory and particular choice of molecular dynamics force field. Finally, the model can be readily applied to a wide range of systems and extended to support other nonlinear spectroscopic techniques, as long as the system–solvent interactions remain weak.

It should be noted that the approach presented here relies heavily on the excitonic band structure that makes it possible to distinguish between low frequency intraband and high frequency interband transitions. These distinctions will no longer be valid in a scenario where molecules are strongly coupled to the solvent, for example, in liquid water, so major modifications will have to be made to treat such systems; in addition, it is not yet clear whether it may be possible use a Markovian QME approach in a strongly coupled system where the bath fluctuations are on the same time scale as the system dynamics and Markovity may not be justified.

It should also be noted that although the linear system–bath coupling mechanism presented here has produced quite satisfactory results, it is not unique. In particular, it would be interesting to test the case of quadratic coupling. Indeed a simulation with quadratic coupling is currently underway and the results will be presented in a future publication. Unlike the linear coupling method, the quadratic coupling equations are greatly simplified by treating the system harmonically.

## ■ AUTHOR INFORMATION

### Corresponding Author

\*E-mail: eitan@umich.edu.

## ■ ACKNOWLEDGMENT

The authors gratefully acknowledge funding from the National Science Foundation [CHE-0748501 (K.J.K.) and CHE-0809506 (E.G.)] as well as a Predoctoral Fellowship from the Rackham Graduate School at the University of Michigan (C.R.B.)

## ■ REFERENCES

- (1) Cho, M. Coherent Two-Dimensional Optical Spectroscopy. *Chem Rev* **2008**, *108*, 1331–1418.
- (2) Jonas, D. M. Two-dimensional femtosecond spectroscopy. *Annu. Rev. Phys. Chem.* **2003**, *54*, 425–463.
- (3) Mukamel, S. Multidimensional femtosecond correlation spectroscopies of electronic and vibrational excitations. *Annu. Rev. Phys. Chem.* **2000**, *51*, 691–729.

- (4) Fayer, M. D. Dynamics of Liquids, Molecules, and Proteins Measured with Ultrafast 2D IR Vibrational Echo Chemical Exchange Spectroscopy. *Annu. Rev. Phys. Chem.* **2009**, *60*, 21.
- (5) Fecko, C. J.; Loparo, J. J.; Roberts, S. T.; Tokmakoff, A. Local hydrogen bonding dynamics and collective reorganization in water: Ultrafast infrared spectroscopy of HOD/D<sub>2</sub>O. *J. Chem. Phys.* **2005**, *122*, 18.
- (6) Bakulin, A. A.; Liang, C.; Jansen, T. L.; Wiersma, D. A.; Bakker, H. J.; Pshenichnikov, M. S. Hydrophobic Solvation: A 2D IR Spectroscopic Inquest. *Acc. Chem. Res.* **2009**, *42*, 1229–1238.
- (7) Roberts, S. T.; Ramasesha, K.; Tokmakoff, A. Structural Rearrangements in Water Viewed Through Two-Dimensional Infrared Spectroscopy. *Acc. Chem. Res.* **2009**, *42*, 1239–1249.
- (8) Nicodemus, R. A.; Ramasesha, K.; Roberts, S. T.; Tokmakoff, A. Hydrogen Bond Rearrangements in Water Probed with Temperature-Dependent 2D IR. *J. Phys. Chem. Lett.* **2010**, *1*, 1068–1072.
- (9) Garrett-Roe, S.; Hamm, P. What Can We Learn from Three-Dimensional Infrared Spectroscopy? *Acc. Chem. Res.* **2009**, *42*, 1412–1422.
- (10) Garrett-Roe, S.; Hamm, P. Three-point frequency fluctuation correlation functions of the OH stretch in liquid water. *J. Chem. Phys.* **2008**, *128*, 104507.
- (11) Callaghan, P. T. *Principles of nuclear magnetic resonance microscopy*; Oxford University Press: New York, 1991.
- (12) Schmidt, J. R.; Roberts, S. T.; Loparo, J. J.; Tokmakoff, A.; Fayer, M. D.; Skinner, J. L. Are water simulation models consistent with steady-state and ultrafast vibrational spectroscopy experiments?. *Chem. Phys.* **2007**, *341*, 143–157.
- (13) Corcelli, S. A.; Lawrence, C. P.; Skinner, J. L. Combined electronic structure/molecular dynamics approach for ultrafast infrared spectroscopy of dilute HOD in liquid H<sub>2</sub>O and D<sub>2</sub>O. *J. Chem. Phys.* **2004**, *120*, 8107–8117.
- (14) Asbury, J.; Steinel, T.; Stromberg, C.; Corcelli, S.; Lawrence, C.; Skinner, J.; Fayer, M. Water dynamics: Vibrational echo correlation spectroscopy and comparison to molecular dynamics simulations. *J. Phys. Chem. A* **2004**, *108*, 1107–1119.
- (15) Oh, K.-I.; Choi, J.-H.; Lee, J.-H.; Han, J.-B.; Lee, H.; Cho, M. Nitrile and thiocyanate IR probes: Molecular dynamics simulation studies. *J. Chem. Phys.* **2008**, *128*, 154504–154510.
- (16) Choi, J. H.; Oh, K. I.; Cho, M. H. Azido-derivatized compounds as IR probes of local electrostatic environment: Theoretical studies. *J. Chem. Phys.* **2008**, *129*, 11.
- (17) Massiot, D.; Fayon, F.; Capron, M.; King, I.; Le Calve, S.; Alonso, B.; Durand, J. O.; Bujoli, B.; Gan, Z. H.; Hoatson, G. Modelling one- and two-dimensional solid-state NMR spectra. *Magn. Reson. Chem.* **2002**, *40*, 70–76.
- (18) Ganim, Z.; Jones, K. C.; Tokmakoff, A. Insulin dimer dissociation and unfolding revealed by amide I two-dimensional infrared spectroscopy. *Phys. Chem. Chem. Phys.* **2010**, *12*, 3579–3588.
- (19) Ganim, Z.; Tokmakoff, A. Spectral signatures of heterogeneous protein ensembles revealed by MD Simulations of 2DIR spectra. *Biophys. J.* **2006**, *91*, 2636–2646.
- (20) Ganim, Z.; Chung, H.; Smith, A.; Deflores, L.; Jones, K.; Tokmakoff, A. Amide I two-dimensional infrared Spectroscopy of proteins. *Acc. Chem. Res.* **2008**, *41*, 432–441.
- (21) Smith, A. W.; Lessing, J.; Ganim, Z.; Peng, C. S.; Tokmakoff, A.; Roy, S.; Jansen, T. L. C.; Knoester, J. Melting of a beta-Hairpin Peptide Using Isotope-Edited 2D IR Spectroscopy and Simulations. *J. Phys. Chem. B* **2010**, *114*, 10913–10924.
- (22) Roy, S.; Jansen, T. L. C.; Knoester, J. Structural classification of the amide I sites of a beta-hairpin with isotope label 2DIR spectroscopy. *Phys. Chem. Chem. Phys.* **2010**, *12*, 9347–9357.
- (23) Jansen, T. L.; Knoester, J. A transferable electrostatic map for solvation effects on amide I vibrations and its application to linear and two-dimensional spectroscopy. *J. Chem. Phys.* **2006**, *124*, 11.
- (24) Jansen, T. L.; Dijkstra, A. G.; Watson, T. M.; Hirst, J. D.; Knoester, J. Modeling the amide I bands of small peptides. *J. Chem. Phys.* **2006**, *125*, 9.
- (25) Khalil, M.; Demirdoven, N.; Tokmakoff, A. Vibrational coherence transfer characterized with Fourier-transform 2D IR spectroscopy. *J. Chem. Phys.* **2004**, *121*, 362–373.
- (26) Nee, M.; Baiz, C.; Anna, J.; McCanne, R.; Kubarych, K. Multi-level vibrational coherence transfer and wavepacket dynamics probed with multidimensional IR spectroscopy. *J. Chem. Phys.* **2008**, *129*, 084503.
- (27) Demirdoven, N.; Khalil, M.; Golonzka, O.; Tokmakoff, A. Correlation effects in the two-dimensional vibrational spectroscopy of coupled vibrations. *J. Phys. Chem. A* **2001**, *105*, 8025–8030.
- (28) Golonzka, O.; Khalil, M.; Demirdoven, N.; Tokmakoff, A. Coupling and orientation between anharmonic vibrations characterized with two-dimensional infrared vibrational echo spectroscopy. *J. Chem. Phys.* **2001**, *115*, 10814–10828.
- (29) Golonzka, O.; Khalil, M.; Demirdoven, N.; Tokmakoff, A. Vibrational anharmonicities revealed by coherent two-dimensional infrared spectroscopy. *Phys. Rev. Lett.* **2001**, *86*, 2154–2157.
- (30) Demirdoven, N.; Khalil, M.; Tokmakoff, A. Correlated vibrational dynamics revealed by two-dimensional infrared spectroscopy. *Phys. Rev. Lett.* **2002**, *89*, 237401.
- (31) Khalil, M.; Demirdoven, N.; Tokmakoff, A. Coherent 2D IR spectroscopy: Molecular structure and dynamics in solution. *J. Phys. Chem. A* **2003**, *107*, 5258–5279.
- (32) Cervetto, V.; Helbing, J.; Bredenbeck, J.; Hamm, P. Double-resonance versus pulsed Fourier transform two-dimensional infrared spectroscopy: An experimental and theoretical comparison. *J. Chem. Phys.* **2004**, *121*, 5935–5942.
- (33) Baiz, C.; Nee, M.; McCanne, R.; Kubarych, K. Ultrafast nonequilibrium Fourier-transform two-dimensional infrared spectroscopy. *Opt. Lett.* **2008**, *33*, 2533–2535.
- (34) Anna, J. M.; Nee, M. J.; Baiz, C. R.; McCanne, R.; Kubarych, K. J. Measuring absorptive two-dimensional infrared spectra using chirped-pulse upconversion detection. *J. Opt. Soc. Am. B* **2010**, *27*, 382–393.
- (35) Baiz, C. R.; McRobbie, P. L.; Preketes, N. K.; Kubarych, K. J.; Geva, E. Two-Dimensional Infrared Spectroscopy of Dimanganese Decacarbonyl and Its Photoproducts: An Ab Initio Study. *J. Phys. Chem. A* **2009**, *113*, 9617–9623.
- (36) Baiz, C. R.; McRobbie, P. L.; Anna, J. M.; Geva, E.; Kubarych, K. J. Two-Dimensional Infrared Spectroscopy of Metal Carbonyls. *Acc. Chem. Res.* **2009**, *42*, 1395–1404.
- (37) Baiz, C. R.; McCanne, R.; Kubarych, K. J. Transient Vibrational Echo versus Transient Absorption Spectroscopy: A Direct Experimental and Theoretical Comparison. *Appl. Spectrosc.* **2010**, *64*, 1037–1044.
- (38) Nee, M. J.; McCanne, R.; Kubarych, K. J.; Joffe, M. Two-dimensional infrared spectroscopy detected by chirped pulse upconversion. *Opt. Lett.* **2007**, *32*, 713–715.
- (39) Mathew, N. A.; Yurs, L. A.; Block, S. B.; Pakoulev, A. V.; Kornau, K. M.; Sibert, E. L.; Wright, J. C. Fully and Partially Coherent Pathways in Multiply Enhanced Odd-Order Wave-Mixing Spectroscopy. *J. Phys. Chem. A* **2010**, *114*, 817–832.
- (40) Pakoulev, A. V.; Rickard, M. A.; Kornau, K. M.; Mathew, N. A.; Yurs, L. A.; Block, S. B.; Wright, J. C. Mixed Frequency-/Time-Domain Coherent Multidimensional Spectroscopy: Research Tool or Potential Analytical Method?. *Acc. Chem. Res.* **2009**, *42*, 1310–1321.
- (41) Pakoulev, A. V.; Rickard, M. A.; Mathew, N. A.; Kornau, K. M.; Wright, J. C. Frequency-domain time-resolved four wave mixing spectroscopy of vibrational coherence transfer with single-color excitation. *J. Phys. Chem. A* **2008**, *112*, 6320–6329.
- (42) Moran, A. M.; Dreyer, J.; Mukamel, S. Ab initio simulation of the two-dimensional vibrational spectrum of dicarbonylacetylacetonato rhodium(I). *J. Chem. Phys.* **2003**, *118*, 1347–1355.
- (43) Haake, F. Statistical treatment of open systems by generalized master equations. *Springer Tracts Mod Phys* **1973**, *66*, 98.
- (44) Alicki, R.; Lendi, K. *Quantum Dynamical Semigroups and Applications*; Springer-Verlag: Berlin, 1987.
- (45) Yoon, B.; Deutch, J. M.; Freed, J. H. A comparison of generalized cumulant and projection operator methods in spin-relaxation theory. *J. Chem. Phys.* **1975**, *62*, 4687.

- (46) Oppenheim, I.; Shuler, K. E.; Weiss, G. H. *Stochastic Processes in Chemical Physics: The Master Equation*; MIT Press: Cambridge, MA, 1977.
- (47) Mukamel, S.; Oppenheim, I.; Ross, J. Statistical reduction for strongly driven simple quantum systems. *Phys. Rev. A* **1978**, *17*, 1988.
- (48) Romero-Rochin, V.; Orsky, A.; Oppenheim, I. Theory of spin relaxation processes. *Physica A* **1989**, *156*, 244.
- (49) Blum, K. *Density matrix theory and applications*; Plenum: New York, 1996.
- (50) Wangsness, R. K.; Bloch, F. The dynamical theory of nuclear induction. *Phys. Rev.* **1953**, *89*, 728.
- (51) Redfield, A. G. On the theory of relaxation processes. *IBM J.* **1957**, *1*, 19.
- (52) van Kampen, N. G. *Stochastic Processes in Physics and Chemistry*; North-Holland: Amsterdam, 1981.
- (53) Kubo, R.; Toda, M.; Hashitsume, N. *Statistical Physics II: Nonequilibrium Statistical Mechanics*; Springer-Verlag: New York, 1985.
- (54) Laird, B. B.; Budimir, J.; Skinner, J. L. Quantum-mechanical derivation of the Bloch equations: Beyond the weak coupling limit. *J. Chem. Phys.* **1991**, *94*, 4391.
- (55) Pollard, W. T.; Felts, A. K.; Friesner, R. A. The Redfield equation in condensed-phase quantum dynamics, *Adv. Chem. Phys.* **1996**, *77*.
- (56) Pollard, W. T.; Friesner, R. A. Solution of the Redfield equation for the dissipative quantum dynamics of multilevel systems. *J. Chem. Phys.* **1994**, *100*, 5054.
- (57) Geva, E.; Kosloff, R.; Skinner, J. L. On the relaxation of a two-level system driven by a strong electro-magnetic field. *J. Chem. Phys.* **1995**, *102*, 8541.
- (58) Geva, E.; Kosloff, R. The quantum heat engine and heat pump: An irreversible thermodynamic analysis of the three-level amplifier. *J. Chem. Phys.* **1996**, *104*, 7681.
- (59) Kohen, D.; Marston, C. C.; J.Tannor, D. Phase space approach to theories of quantum dissipation. *J. Chem. Phys.* **1997**, *107*, 5236.
- (60) Cao, J. Phase space study of Bloch-Redfield theory. *J. Chem. Phys.* **1997**, *107*, 3204.
- (61) Yan, Y. J. Quantum Fokker-Planck theory in a non-Gaussian-Markovian medium. *Phys. Rev. A* **1998**, *58*, 2721.
- (62) Berman, M.; Kosloff, R.; Tal-Ezer, H. Solution of the time-dependent Liouville-von Neumann equation: Dissipative evolution. *J. Phys. A* **1992**, *25*, 1283.
- (63) Ashkenazi, G.; Banin, U.; Bartana, A.; Kosloff, R.; Ruhman, S. Quantum description of the impulsive photodissociation dynamics of I3 in solution. *Adv. Chem. Phys.* **1997**, *100*, 229.
- (64) Ashkenazi, G.; Kosloff, R.; Ratner, M. A. Photoexcited electron transfer: Short time dynamics and turnover control by dephasing relaxation and control. *J. Am. Chem. Soc.* **1999**, *121*, 3386.
- (65) Kosloff, R.; Ratner, M. A.; Davis, W. B. Dynamics and relaxation in interacting systems: Semigroup approach. *J. Chem. Phys.* **1997**, *106*, 7036.
- (66) Suarez, A.; Silbey, R. Hydrogen tunneling in condensed media. *J. Chem. Phys.* **1991**, *94*, 4809.
- (67) Li, D.; Voth, G. A. Feynman path integral approach for studying intramolecular effects in proton-transfer reactions. *J. Phys. Chem.* **1991**, *95*, 10425.
- (68) Skinner, J. L.; Park, K. Calculating Vibrational Energy Relaxation Rates from Classical Molecular Dynamics Simulations: Quantum Correction Factors for Processes Involving Vibration-Vibration Energy Transfer. *J. Phys. Chem. B* **2001**, *105*, 6716–6721.
- (69) Everitt, K. F.; Geva, E.; Skinner, J. L. Determining the solvation correlation function from three-pulse photon echoes in liquids. *J. Chem. Phys.* **2001**, *114*, 1326.
- (70) Ka, B. J.; Geva, E. A nonperturbative calculation of nonlinear spectroscopic signals in liquid solution. *J. Chem. Phys.* **2006**, *125*, 214501.
- (71) Mukamel, S. *Principles of nonlinear optical spectroscopy*; Oxford University Press: New York, 1995.
- (72) Becke, A. D. Density-functional exchange-energy approximation with correct asymptotic behavior. *Phys. Rev. A* **1988**, *38*, 3098.
- (73) Perdew, J. P. Density-functional approximation for the correlation energy of the inhomogeneous electron gas. *Phys. Rev. B* **1986**, *33*, 8822.
- (74) Hay, P. J.; Wadt, W. R. Ab initio effective core potentials for molecular calculations. Potentials for the transition metal atoms Sc to Hg. *J. Chem. Phys.* **1985**, *82*, 270–283.
- (75) Adams, D. M.; Hooper, M. A.; Squire, A. A Raman spectroscopic study of dimanganese and dirhenium decacarbonyls. *J. Chem. Soc. A* **1971**, 71–77.
- (76) Wang, J.; Wang, W.; Kollman, P. A.; Case, D. A. Automatic atom type and bond type perception in molecular mechanical calculations. *J. Mol. Graph. Model.* **2006**, *25*, 247–260.
- (77) Baiz, C. R.; McCanne, R.; Nee, M. J.; Kubarych, K. J. Orientational Dynamics of Transient Molecules Measured by Nonequilibrium Two-Dimensional Infrared Spectroscopy. *J. Phys. Chem. A* **2009**, *113*, 8907–8916.
- (78) Ryckaert, J.-P.; Ciccotti, G.; Berendsen, H. J. C. Numerical integration of the cartesian equations of motion of a system with constraints: molecular dynamics of n-alkanes. *J. Comput. Phys.* **1977**, *23*, 327–341.
- (79) Van Der Spoel, D.; Lindahl, E.; Hess, B.; Groenhof, G.; Mark, A. E.; Berendsen, H. J. C. GROMACS: Fast, flexible, and free. *J. Comput. Chem.* **2005**, *26*, 1701–1718.
- (80) Oglivie, J. P.; Kubarych, K. J. Chapter 5 Multidimensional Electronic and Vibrational Spectroscopy: An Ultrafast Probe of Molecular Relaxation and Reaction Dynamics. *Adv. At. Mol. Opt. Phys.* **2009**, *57*, 249–321.
- (81) Engel, G. S.; Calhoun, T. R.; Read, E. L.; Ahn, T. K.; Mancal, T.; Cheng, Y. C.; Blankenship, R. E.; Fleming, G. R. Evidence for wavelike energy transfer through quantum coherence in photosynthetic systems. *Nature* **2007**, *446*, 782–786.
- (82) Lee, H.; Cheng, Y. C.; Fleming, G. R. Coherence dynamics in photosynthesis: Protein protection of excitonic coherence. *Science* **2007**, *316*, 1462–1465.
- (83) Mukamel, S. Communications: Signatures of quasiparticle entanglement in multidimensional nonlinear optical spectroscopy of aggregates. *J. Chem. Phys.* **2010**, *132*, 241105.
- (84) Collini, E.; Wong, C. Y.; Wilk, K. E.; Curmi, P. M. G.; Brumer, P.; Scholes, G. D. Coherently wired light-harvesting in photosynthetic marine algae at ambient temperature. *Nature* **2010**, *463*, 644–U669.
- (85) Abramavicius, D.; Mukamel, S. Quantum oscillatory exciton migration in photosynthetic reaction centers. *J. Chem. Phys.* **2010**, *133*, 9.

## NOTE ADDED IN PROOF

We have carried out new simulations which explicitly include the frequency dependence of the force–force correlation function (Figure 5, inset). No qualitative difference in the peak dynamics was observed.